AIAA Journal, Volume 61, Issue 1, January 2023, pp. 217-284
DOI:10.2514/1.J061917

Hilbert-Huang spectral analysis of cavity flows incorporating fluidic spoilers

David Bacci,* Alistair J. Saddington†

Cranfield University, Shrivenham, Swindon, SN6 8LA, UK

Numerical aero-acoustic analysis was conducted on an M219 cavity geometry, incorporating signature suppression features and leading-edge fluidic spoilers. The numerical model was validated against existing experimental data. The palliative properties of fluidic spoilers were investigated at Mach numbers of 0.85, 1.20 and 1.80 with blowing coefficients of 0.03 and 0.06. Results are presented for the acoustic spectrum and further analysis was conducted using the Hilbert-Huang methodology. The fluidic spoilers were able to reduce considerably the overall level of acoustic noise and to reduce and/or suppress the resonant modes typical of cavity flows. The effectiveness of the spoilers was a direct consequence of their effect on the detached shear layer, of which the trajectory and coherence was altered. The Hilbert-Huang spectral analysis provided an enhanced understanding of the complex nature of the aero-acoustic behavior of the cavity. Acoustic modes were identified that, together with the Rossiter-Heller tones, govern the behavior of the spectrum. This demonstrated how the generated tones, appearing inside the cavity, were a result of complex non-linear interactions between shear layer acoustic instabilities and centrifugal instabilities originating in the flow recirculating in the internal part of the cavity. This also demonstrated that the fundamental frequencies had frequency and amplitude modu-

*Visiting Research Fellow. Aeromechanical Systems Group, Centre for Defence Engineering.

†Reader in Aeromechanical Systems. Aeromechanical Systems Group, Centre for Defence Engineering. Corresponding author (a.j.saddington@cranfield.ac.uk)

lation characteristics that spread the energy in a wide bandwidth. This is not captured by classical Fourier analysis.

Keywords: cavity; aeroacoustic; transonic; supersonic; fluidic; spoiler

Nomenclature

C_μ	blowing coefficient
D	cavity depth [m]
d	fluidic spoiler duty cycle (l/λ)
f	frequency [Hz]
f_a	fundamental frequency loop [Hz]
f_b	amplitude modulation frequency [Hz]
f_n	frequency of the nth Rossiter-Heller mode [Hz]
f_r	frequency resolution [Hz]
f_s	sampling frequency [Hz]
g	spanwise spacing between individual slot-jets [mm]
h	slot-jet streamwise extent [mm]
K	velocity ratio in Eqn. 1
L	cavity length [m]
l	spanwise slot-jet length [mm]
M	Mach number
M_n	nth Rossiter-Heller mode
M_{CI_n}	nth Rossiter-Heller mode generated by centrifugal instability
M_{TI_n}	nth Rossiter-Heller mode generated by transverse instability
$\dot{m}$	mass flow rate [kgs^{-1}]
n	number of slots; index in Eqn. 1.
p	static pressure [Pa]
t	time [s]

t_c	convective time (L/U_∞)
U	flow speed [ms^{-1}]
W	cavity width [m]
γ	ratio of specific heats
δ_0	boundary layer thickness at the cavity leading edge [m]
λ	wavelength of the slot-jet [mm]
ξ	amplitude modulation parameter, phase lag in Eqn. 1
ρ	fluid density [kgm^{-3}]
ρ_P	Pearson's linear correlation coefficient
σ	root mean square

Abbreviations

AM	amplitude modulation
CFD	computational fluid dynamics
CFL	Courant-Friedrichs-Lewy condition
EEMD	ensemble empirical mode decomposition
FM	frequency modulation
IMF	intrinsic mode function
LES	large eddy simulation
OASPL	overall sound pressure level [dB]
PSD	power spectral density
RANS	Reynolds-Averaged Navier-Stokes
SPL	sound pressure level [dB]
VMD	variational mode decomposition

Subscript

j	fluidic spoiler exit conditions
∞	freestream conditions

I. Introduction

Design requirements for modern military aircraft are strongly influenced by the necessity to minimize the radar signature and to reduce aerodynamic drag, especially in the transonic and supersonic flight regimes. These requirements lead to the installation of weapon bays in the fuselage of military aircraft. During weapon release, when the bay doors are opened and the cavity is exposed to high speed flow, an acoustic field develops with unsteady pressure levels with the potential to damage the airframe and the payload. Additionally, the local flow poses a hazard for the release of the weapon. As shown by Rockwell and Naudasher [1], these phenomena are dependent on the cavity geometry and the freestream conditions. In particular situations the pressure oscillations can also coalesce into resonant modes. The frequencies at which resonance occurs are called Rossiter modes, following early work on cavity flows [2]. The resonant frequencies are more generally predicted using the following Rossiter-Heller equation [3], which accounts for Mach number effects.

$$f_n = \frac{U_\infty}{L} \cdot \frac{n - \xi}{M_\infty \left[1 + \frac{(\gamma-1)}{2} {M_\infty}^2\right]^{-\frac{1}{2}} + \frac{1}{K}} \tag{1}$$

Here K is the ratio of the disturbance velocity in the shear layer to the freestream velocity (generally taken as 0.57), and ξ is an empirical constant employed to account for the phase lag between the passage of an eddy past the cavity trailing edge and the formation of an upstream traveling disturbance. The value of ξ depends on the length-to-depth ratio, L/D, of the cavity and is evaluated as $\xi = 0.062(L/D)$ [2]. The ratio of specific heats, γ, is assumed to be equal to 1.4 for air.

As shown by Delprat [4], it is possible to express the resonating frequencies as the result of an amplitude modulation of a fundamental acoustic tone and its harmonics. From this the Rossiter-Heller modes can be expressed as,

$$f_n = (n - \xi) \cdot \left[f_a \pm k\Delta f\right] \quad n = 1, 2, 3, \ldots \tag{2}$$

Here f_a is the fundamental frequency loop of the cavity (also called the 'carrier frequency'); ξ is the amplitude modulation parameter, or the ratio of the amplitude modulation frequency, f_b, to f_a;

Δf is the modulating frequency (which usually coincides with the lowest frequency peak in the spectrum); and k is an integer. Knowing that the Rossiter-Heller equation does not consider the modulating frequency, Δf, it is possible to combine Eqns. 1 and 2 and extract the direct dependence of f_a and f_b on the cavity geometry and freestream conditions as follows.

$$f_a = \frac{U_\infty}{L} \cdot \frac{1}{M_\infty \left[1 + \frac{(\gamma-1)}{2} {M_\infty}^2\right]^{-\frac{1}{2}} + \frac{1}{K}} \tag{3}$$

$$f_b = \frac{U_\infty}{D} \cdot \frac{0.062}{M_\infty \left[1 + \frac{(\gamma-1)}{2} {M_\infty}^2\right]^{-\frac{1}{2}} + \frac{1}{K}} \tag{4}$$

$$\xi = \frac{f_b}{f_a} = 0.062 \left(\frac{L}{D}\right) \tag{5}$$

Subsequent studies [5–7] associated this set of frequencies with fluid structures inside the cavity. A typical open-type cavity, in which resonant frequencies are expected to appear, is characterized by a detached shear layer that forms at the leading edge of the cavity and impinges on the downstream wall. Additionally, a recirculation region, typically defined by one or more eddies, is present inside the cavity. The resonance phenomenon is usually associated with the cavity fundamental frequency, f_a, and is strongly dependent on cavity length, with Strouhal numbers (based on cavity depth, D) greater than or equal to 0.2. The fundamental frequency is typically phase locked and is affected by non-linear saturation phenomena, that convey energy towards associated harmonics.

The low frequency values $k\Delta f$, responsible for the frequency modulation mechanism [4, 7], are generated by the internal cavity flow and, more precisely, by centrifugal instabilities in the recirculating flow. Typical Strouhal numbers range from 0.005 to 0.05, depending on the source mechanism. Low Strouhal numbers are usually associated with velocity fluctuations in the layers of the recirculating flow inside the cavity, whereas higher modes are associated to the formation of sub-eddies inside the stratified layers of the main vortex. The interaction of these centrifugal instabilities with the acoustic modes of the shear layer are via a non-linear quadratic coupling [5, 6, 8, 9] and are responsible for the generation of the Rossiter-Heller tones.

A third type of wave pattern can develop inside the cavity, which is related to the three-

dimensionality of the flow. These are referred to as transverse instabilities, or spanwise induced oscillations, and are the result of the non-linear interaction between the shear layer and the centrifugal instabilities and have Strouhal numbers typically between 0.1 to 0.2, for cavities with W/D of the order of one [7]. The associated structures are helical coils (with longitudinal axes) winding up around the inner recirculating flow.

Flow control methods offer the possibility of suppressing the aero-acoustic phenomena in both subsonic [10–14] and supersonic [15–24] applications. The control method can be either passive [11–13, 15, 16, 20, 22, 25–27] or active [10, 14, 18, 19, 21, 24, 28–34]. Typical passive control methods, of which leading edge spoilers are the most common[a], have proven to be effective in suppressing the resonant tones and reducing the acoustic loads (see Thangamani et al. [11] for an analysis of various passive control methods). Spoilers have a fixed design point and, as a consequence, the palliative effect may not be consistent across the flight envelope; in some cases worsening the level of acoustic loads. Additionally, spoilers exposed to the freestream increase the radar signature and profile drag of the aircraft. Active control mechanisms, which use external energy to alter the flow, offer a more flexible approach (see Cattafesta et al. [30] for a review on active control of cavity flows). Previous studies have indicated that fluid injection at the cavity leading edge, can provide considerable acoustic noise suppression over a wide range of Mach numbers. For example, Mendoza and Ahuja [31] obtained a reduction of up to 30 dB by injecting air normal to the freestream flow, and Ukeiley et al. [32], using slot-jets at the cavity leading edge, demonstrated the possibility of suppressing resonant tones and reducing acoustic loads by up to 50% at supersonic speeds. Lusk et al. [18] obtained similar results at supersonic speeds; the most successful used a configuration of five slot-jets and a blowing coefficient, C_μ of 0.0128.

Zhang et al. [14] conducted a comprehensive analysis to understand the effects of flow control using steady slot-jets placed in proximity to a cavity leading edge exposed to Mach 0.3-0.7 flow. They observed that this type of control is able to suppress aeroacoustic phenomena due to two co-existing effects: the lifting of the shear layer, that is diverted away from the cavity; the generation of 3-d disturbances, in the shape of horseshoe vortices, that alter the coherent structure of the

[a]Leading-edge spoilers have been used as a flow control mechanism on a number of in-service aircraft.

shear layer, resulting in the reduction of the integral scale of the turbulence detaching from the leading edge. Hence, the strength of the acoustic noise generation mechanism is reduced. In their experiments Zhang et al. [14] derived some guidelines regarding the optimum blowing coefficient and the spatial arrangement of the slots, within which the beneficial effects were observed. Similar acoustic noise suppression capabilities were demonstrated, at supersonic speeds, by Turpin et al. [24].

Although steady blowing has proven to be effective in reducing cavity noise, the geometry used in previous studies was a simple rectangular cavity, however, complex-geometry cavities, representative of aircraft applications, can exhibit behaviors different to the idealized case [35−37].

The present work seeks to explore the effectiveness of fluidic spoilers installed in the leading edge of a weapon bay geometry incorporating typical low-observable features. Numerical analyses were conducted using the scale-adaptive-simulations (SAS) turbulence model. The effectiveness of the spoilers was tested at transonic and supersonic Mach numbers (0.85, 1.20, 1.80) in order to assess the performance at flight conditions typical of modern military aircraft.

II. Cavity geometry

The cavity model was derived from the well-known M219 geometry [38], which has a length-to-depth ratio (L/D) of five and a width-to-depth ratio (W/D) of one (Fig. 1). The M219 cavity is, however, not representative of typical geometries present on military aircraft. Low-observable (LO) aircraft incorporate saw-tooth leading and trailing edges on the doors and associated fuselage indentations. Hence, whilst the validation of the numerical procedures was conducted on an M219 geometry, since for this configuration experimental data was available, a new cavity model was developed that included leading and trailing edge indentations.

The new geometry (Fig. 2), referred to as v2w000, introduced a double chevron step of 5 mm depth at the front and rear walls. The angle of the indentations was set at 45 degrees, typical of that present on LO aircraft. The step height was chosen to provide enough room to accommodate the bay doors in their closed position [39, 40].

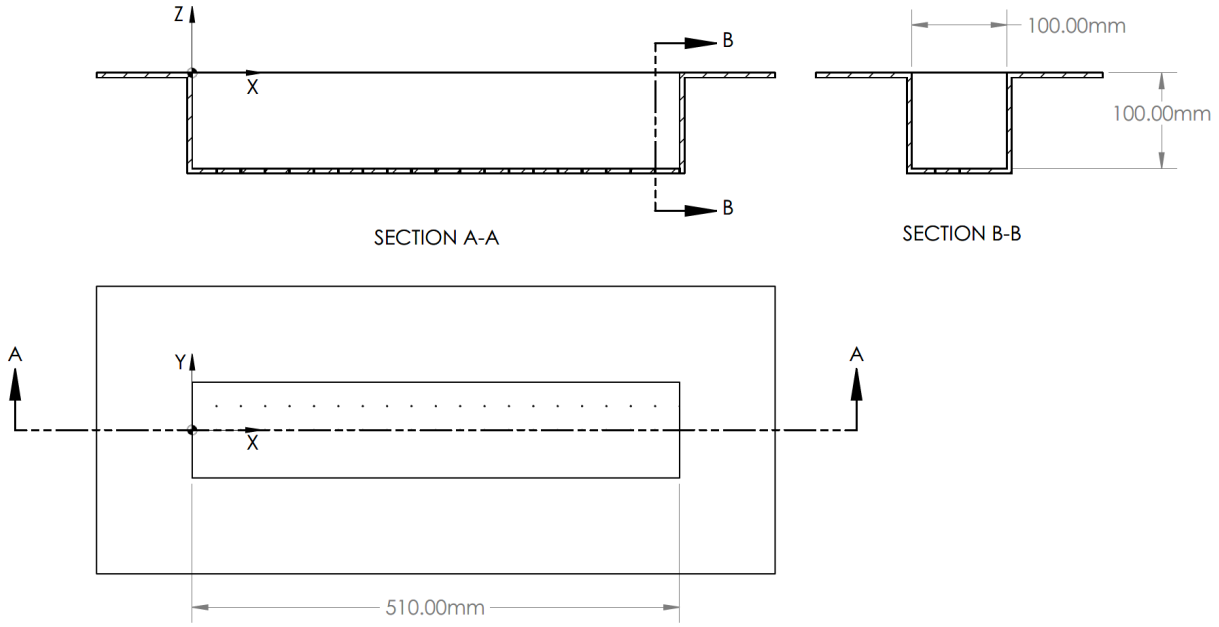

Figure 1: Three-view drawing of the M219 cavity from Henshaw [38].

A. Fluidic spoilers

Recent publications on cavity active flow control have demonstrated that the introduction of steady jets at the cavity leading edge are highly effective at acoustic load suppression [18, 41, 42]. In their combined experimental and computational study Zhang et al. [14] provided guidelines for fluidic spoiler configurations and power settings and showed how multiple-slot arrangements obtained higher suppression levels than a single continuous one. As show in Fig. 3, the principal parameters of the leading-edge slots are the spanwise length, l, the spanwise spacing between slots, g, the wavelength, λ, and the blowing coefficient C_μ, defined as,

$$C_\mu = \frac{\overline{\dot{m}_j U_j}}{0.5\rho_\infty {U_\infty}^2 W \delta_0} \tag{6}$$

Here $\dot{m}_j$ represents the total mass flow injected into the domain by the fluidic spoilers, U_j the average ejection velocity, δ_0 the boundary layer thickness, and the overbar is the time-mean operator.

Lusk et al. [18] and George et al. [42] demonstrated that a five-slot configuration was more effective at reducing the cavity noise than a three-slot or single-slot configuration. Both studies were

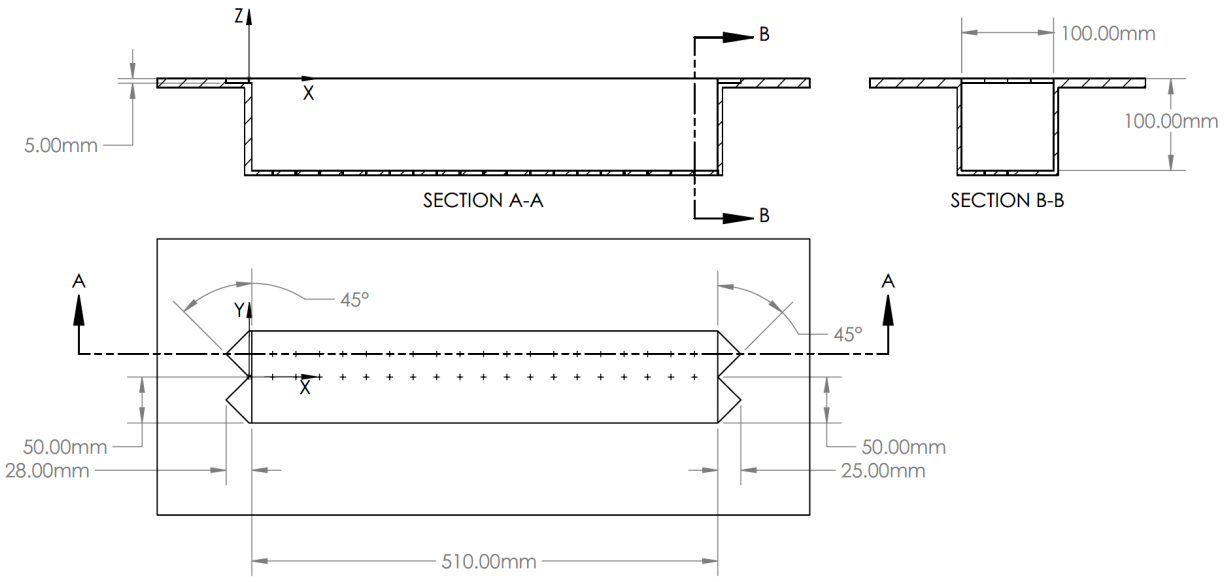

Figure 2: Three-view drawing of the modified M219 cavity (v2w000).

conducted with a freestream Mach number of 1.4. Additionally, Zhang et al. [14] demonstrated that for Mach numbers from 0.3 to 0.7 the highest noise reduction was observed with a five-slot geometry having a spatial duty cycle ($d = l/\lambda$) of 0.25 and a blowing coefficient of at least 0.025, with a value of 0.05 as the threshold above which the noise reduction reaches a plateau. Based on these findings, the current study uses a five-slot leading-edge fluidic spoiler with the geometric parameters specified as: $l = 5.5$ mm; $g = 16.5$ mm; $h = 1.0$ mm; $\lambda = 22.0$ mm; and a duty cycle of 0.25. The slots were installed inside the sawtooth-shaped step at the front of the cavity, as shown in Fig. 4. This solution was selected in order to comply with LO requirements.

III. Numerical methodology and validation

A. Methodology

The simulations in this study were performed using the SST-SAS turbulence model [43] within the ANSYS Fluent R19.2 CFD code. The capability of this code and the turbulence model to properly address transonic cavity flow has been demonstrated by Egorov et al. [44].

An unstructured tetrahedral-type mesh was used with a prism layer wrapped around the viscous

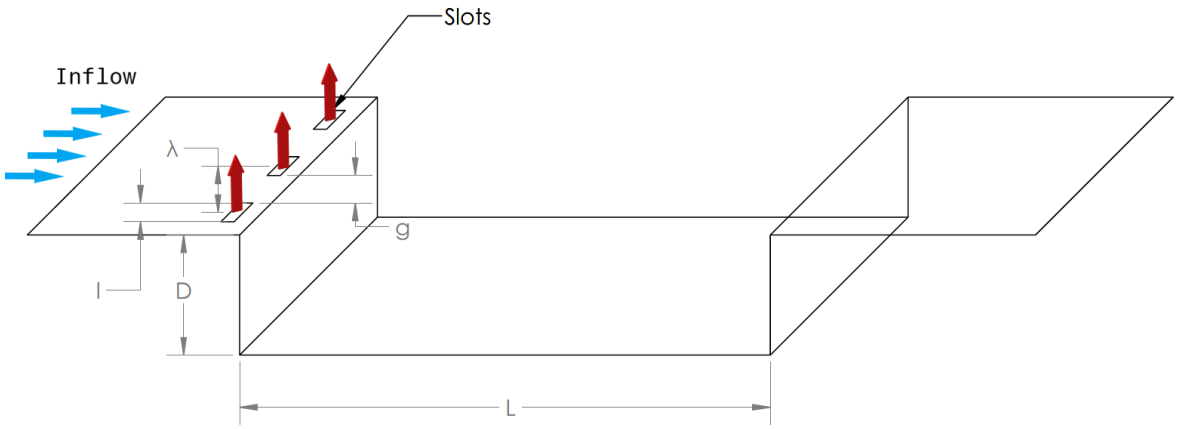

Figure 3: Schematic of the fluidic spoilers showing the principal geometric parameters.

surfaces for accurate boundary layer resolution. The critical areas were the shear layer detaching from the cavity leading edge and the flow inside the cavity. For accurate shear layer modeling with scale-resolving simulations the detached shear layer was resolved using a spacing equal to 0.05 times its minimum thickness (i.e. at the cavity leading edge), as suggested by Menter [45]. All solid walls were specified as adiabatic surfaces where the no-slip condition was applied. The computational outer boundary was specified as a far-field, using the modified Riemann invariants condition. The fluidic spoilers were modelled as a pressure inlet boundary condition with constant values of total pressure, temperature, and static pressure. The computational domain (Fig. 5) consisted of a cavity placed flush within a planar surface, extending $1.5L$ upstream and downstream of the cavity and $4D$ laterally. The no-slip wall was surrounded by a frictionless (symmetry) wall extending $2L$ upstream and downstream. The overall domain extended for $8L$ in the streamwise direction, $29D$ in the transverse direction, and $5L$ in the vertical direction. The dimensions of the computational domain have been validated in previous studies [46], hence no domain sensitivity analysis was conducted for this case.

The air was treated as an ideal compressible gas using Sutherland's law for viscosity modeling. Due to the compressible nature of the problem a pressure-based coupled (in momentum and continuity) solver was used. Non-viscous fluxes were resolved using second order schemes: the

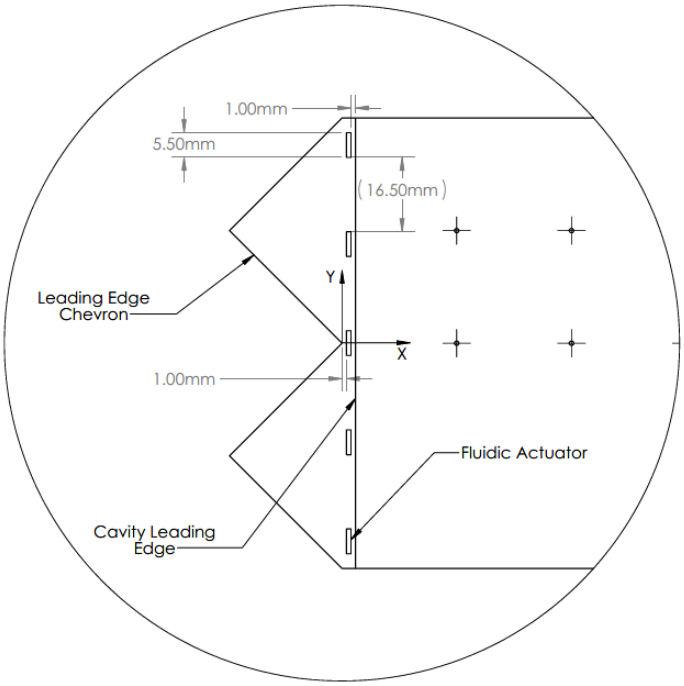

Figure 4: Schematic and principal dimensions of the fluid spoilers installed in the v2w000 geometry.

second-order upwind scheme for density and energy [47]; the standard second order central difference scheme for pressure; and the bounded central differencing scheme for momentum [48]. These settings were in line with previous studies on similar applications and already validated for strongly separated flows and acoustics [43–45]. Viscous fluxes (the terms for k and ω) were resolved using a second-order upwind scheme [47], whilst dissipative/diffusive terms were discretized using a second-order central difference scheme, and gradients were evaluated using the least squares method. The time marching scheme was an implicit second-order dual-time formulation. Temporal discretisation used the standard bounded second-order scheme. Five inner sub-iterations were found to be adequate, which is consistent with the recommendation of Menter [45] and the approaches of Chaplin and Birch [49] and Bacci et al. [9].

As advised by Menter [45], the time step was chosen to ensure a CFL number approximately equal to unity in the LES part of the domain. Unsteady simulations were initiated from a converged RANS solution to reduce the start-up time. To resolve accurately all of the main features the simulation was run for a total of 250 convective times ($t_c = L/U_\infty$), discarding the initial $100t_c$

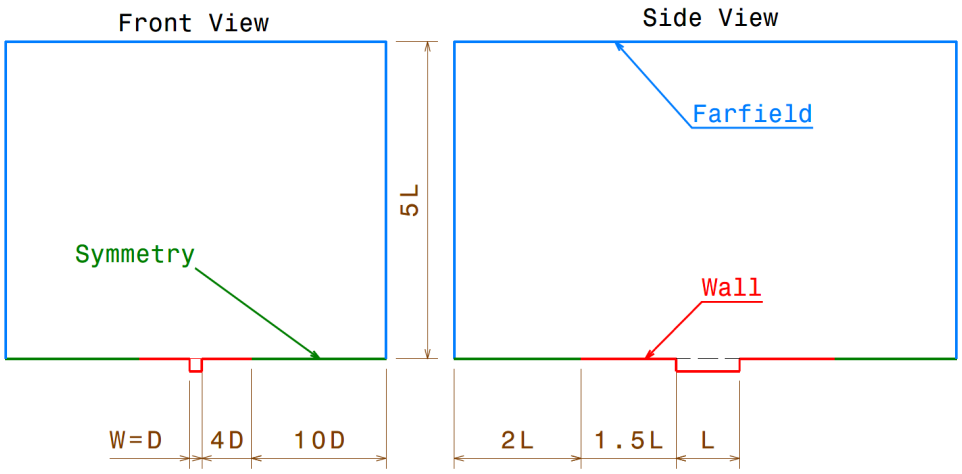

Figure 5: Boundary conditions and dimensions of the computational domain.

seconds to clear the solution from the start-up transient. This allowed data sample lengths greater than 30 cycles of the lowest frequency mode of interest (first Rossiter-Heller Mode) in accordance with the values suggested by Menter [45].

B. Validation

To validate the computational settings and mesh convergence, data were used from wind tunnel studies of the M219 cavity [38] and compared against a computational model of the same geometry. Four meshes were developed (coarse, medium, fine, and extra-fine), and the results compared to the experimental data (Fig. 6). There are small differences in the OASPL, which was defined as,

$$\mathrm{OASPL} = 20\log_{10}\left(\frac{\sigma_p}{p_{\mathrm{ref}}}\right) \tag{7}$$

where p_{ref} is the minimum audible pressure, defined as the threshold of human hearing, and equal to 2×10^{-5} Pa.

The differences are of the order of 1 dB, between the fine and extra-fine results, which is within the error band of the experimental data. The level of agreement between the fine and extra-fine grids was sufficient to consider that the fine grid produced a grid-converged solution. This is consistent with similar transonic cavity flow studies [39, 50]. The fine mesh consisted of 32.1 million elements, of which 16.4 million were located inside the cavity. The computational domains for all the other

geometries were constructed following the same approach.

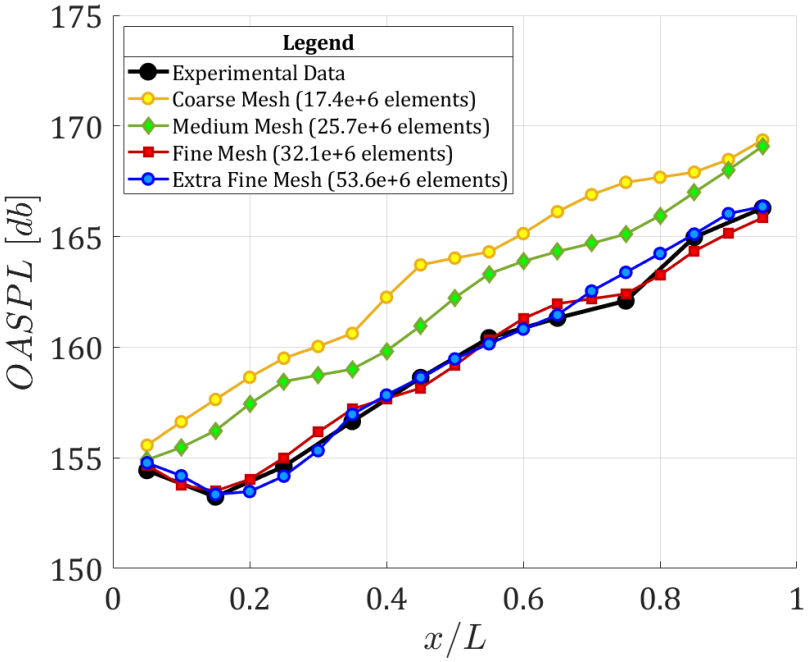

Figure 6: CFD grid convergence based on centerline OASPL showing comparison with experimental data [38].

C. Test matrix

Three different Mach numbers (0.85, 1.20, 1.80) were selected to evaluate the fluidic spoiler performance. These were chosen to represent the range of flight conditions under which the cavity would be exposed to the freestream. In all cases the freestream total pressure and total temperature were 101325 Pa and 300 K respectively. Together with the reference case, where the fluidic spoilers were not activated ($C_\mu = 0.0$), two additional values of blowing coefficient were tested: 0.03 and 0.06. These were selected following the study of Zhang et al. [14], where it was demonstrated that suppression of acoustic noise improved considerably with blowing coefficients above 0.02 and reached a plateau at 0.05.

IV. Data analysis methods

The non-stationary flow analysis involved both frequency and time-frequency domains. For the frequency domain analysis the sound pressure level (SPL) of the fluctuating part of the pressure signal was calculated as [9],

$$\mathrm{SPL}(f) = 10\log_{10}\left(\frac{\mathrm{PSD}_{p_f}(f)\cdot\Delta f_{\mathrm{ref}}}{{p_{\mathrm{ref}}}^2}\right) \tag{8}$$

where, Δf_{ref} is a reference frequency set equal to 1 Hz. In this study the power spectral density (PSD) was obtained using the Welch method [51]. The original signal was divided into smaller blocks with 50 % overlap. The number of samples was equal to the ratio f_s/f_r, where f_s is the sampling frequency (10 kHz) and f_r is the frequency resolution (20 Hz). A Hanning window was then applied to each block to reduce leakage effects. Finally, the PSD of the original signal was calculated by averaging the square of the PSD of each block.

Typically, aerodynamic data, whether from experiments or numerical modeling, are characterized by non-stationary (from a statistical point of view) and non-linear processes. Historically, the fast Fourier transform (FFT), or methodologies based on this, has provided a general method for examining the global energy-frequency distributions. However, the FFT assumes that the analyzed dataset represents a linear system, and the phenomenon under analysis is statistically stationary.

The non-linear nature of turbulence implies that Fourier spectral analysis is of limited use. Firstly, the Fourier spectrum defines uniform harmonic components globally, requiring many additional harmonic components to simulate non-stationary data that are non-uniform. As a result it spreads the energy over a wide frequency range. For example, a sudden change (typically observed in the mode switching phenomenon of cavity flows), is translated into a uniform white noise, with negative and positive frequencies. Another drawback is the fact that Fourier spectral analysis uses linear superposition of trigonometric functions, requiring additional harmonic components to simulate deformed wave profiles. Such deformations, which are a direct consequence of non-linear effects, are then misinterpreted.

Whenever the form of the data deviates from a pure sine or cosine function, the Fourier spectrum

will contain harmonics that are not a true feature but simply a mathematical consequence of applying a linear decomposition method to a nonlinear dataset. Methods have been developed to improve analysis of nonlinear datasets including the short-time Fourier transform and the wavelet transform, however, they still require the dataset to be linear and fail to satisfy two requirements pivotal for the analysis of a non-linear/non-stationary dataset i.e., locality and adaptivity. The requirement for locality is the most crucial for non-stationarity data as there is no time scale; therefore, all events must be identified by the time of their occurrences (that is energy and frequency are functions of time). The requirement for adaptivity is also crucial. Only by adapting to the local variations of the data can the decomposition account fully for the underlying physics of the processes. This is especially important for the nonlinear phenomena, since a manifestation of nonlinearity is a 'harmonic distortion' in the Fourier analysis.

To address these issues, Huang et al. [52] proposed the Hilbert-Huang spectrum, which comprises two steps. First, the data is pre-processed by the empirical mode decomposition method, which extracts several intrinsic mode function (IMF) components. This expands the original time series on a basis that is derived from the data, satisfying the requirement for adaptivity. Secondly, the Hilbert transform is applied to the decomposed IMFs to construct the energy-frequency-time distribution, known as the Hilbert spectrum, in which the time localities of events are preserved.

Several methods have been developed for the determination of the IMFs. In this study two techniques have been selected, due to their successful application to the analysis of datasets with similar behavior to the pressure fluctuations in cavity flows. These methods are the ensemble empirical mode decomposition (EEMD) [53] and the variational mode decomposition (VMD) [54]. The former is based on a procedure called sifting. This is an iterative procedure to extract the IMF that is stopped when the residual becomes a monotonic function. The extracted IMFs must have only one extreme between zero crossing and must have a zero-mean value. The VMD procedure decomposes the signal into a series of narrowband functions, such that each IMF can be expressed as a simple amplitude modulation (AM) and frequency modulation (FM) wave. Additionally, each mode has a positive slowly varying envelope; in case this condition is not satisfied, the mode is further divided until convergence is obtained. Typically the EEMD procedure is computationally faster, but may

produce IMFs of no physical significance. The VMD method is a slower computational procedure but it can produce better results, even if its accuracy is strongly dependent on parameters that must be selected before the decomposition. Each procedure has strengths and weaknesses and shall be applied accordingly. A typical approach is the characterization of the signal using EEMD and the subsequent application of VMD to a sub-ensemble of the obtained IMFs.

Given a signal, $x(t)$, of temporal length, T, it is possible to write,

$$x(t) = \sum_{i=1}^{n} \mathrm{IMF}_i(t) + r_n(t) \tag{9}$$

Here, $r_n(t)$ is the residual after the decomposition in n modes. The next step is to apply the Hilbert transform to each IMF, and derive the analytical signal $z(t)$ of $x(t)$ as,

$$z(t) = \sum_{i=1}^{n} \mathrm{IMF}_i(t) + jH\left[\sum_{i=1}^{n} \mathrm{IMF}_i(t)\right] = \sum_{i=1}^{n} a_i(t) e^{j\theta_i(t)} \tag{10}$$

and,

$$H\langle x(t)\rangle = \frac{1}{\pi} P \int_{-\infty}^{+\infty} \frac{x(t')}{t-t'}\,\mathrm{d}t \tag{11}$$

Eqn. 11 is the definition of the Hilbert transform, where P is the Cauchy principal value. From Eqn. 10 it is possible to express each IMF in terms of its instantaneous amplitude, $a_i(t)$, and phase, $\theta_i(t)$, from which the instantaneous frequency, $f_i(t)$, follows as,

$$f_i(t) = \frac{\omega_i(t)}{2\pi} = \frac{1}{2\pi}\frac{\partial \theta_i(t)}{\partial t} \tag{12}$$

The Hilbert spectrum is then defined as,

$$H(\omega,t) = \sum_{i=1}^{n} H_i(\omega,t) \tag{13}$$

and

$$H_i(\omega,t) = \begin{cases} |a_i(t)|, & \omega = \omega_i(t) \\ 0, & \text{otherwise} \end{cases} \tag{14}$$

This definition enables the representation of the amplitude and the instantaneous frequency as a function of time in a 3-dimensional plot, in which the amplitude can be contoured in the frequency-time plane. This frequency-time distribution of the amplitude is defined as the Hilbert spectrum, $H(\omega,t)$, with the associated Hilbert spectral energy $H_e(\omega,t) = H^2(\omega,t)$. It is possible to see that each IMF represents an intrinsic feature of the signal and, if properly calculated, describes a physical phenomenon [52].

From the Hilbert spectrum it is possible to define the Hilbert marginal spectrum, $h(\omega)$ as,

$$h(\omega) = \int_0^T H(\omega,t)\,\mathrm{d}t \tag{15}$$

This quantity represents the cumulative amplitude over the entire data span in a probabilistic sense. In the Hilbert spectrum, the presence of a peak at a frequency bin has a different meaning from the Fourier spectral analysis. In the Fourier representation, the existence of energy at a given frequency indicates that a component of a sine or cosine wave persisted through the time span of the data. In the Hilbert marginal spectrum, the existence of energy at a given frequency indicates that in the whole timespan of the data there is a higher likelihood that such a wave appeared locally.

It is useful to introduce a measure of the acoustic power expressed by each IMF. This new quantity, referred to as the IMF-associated OASPL (IOASPL), is expressed as,

$$\mathrm{IOASPL} = 20\log_{10}\left(\frac{\sigma_{\mathrm{IMF}_i}}{p_{\mathrm{ref}}}\right) \tag{16}$$

A. Validation of the Hilbert-Huang time-spectral analysis methodology

Initially, the Hilbert-Huang spectral analysis was applied to the experimental data of Henshaw [38]. This provided a benchmark for the data processing technique and it was used to validate and consolidate the procedure.

The EEMD and VMD decomposition algorithms have strengths and weaknesses [55]. To separate components, EEMD requires that the ratio of two consecutive features are smaller than 0.75 (lower frequency to higher frequency ratio), with optimal values below 0.5. On the other hand, the principal drawbacks of VMD are its sensitivity to white and colored noise (if the signal-to-noise ratio is not high enough), and the requirement that components can be identified in the frequency spectrum (i.e. defined tones are present). To analyze the pressure signals from the cavity flows, and to determine what IMF to keep or discard, the following procedure was applied.

- The initial signal, $x(t)$ was decomposed using the EEMD procedure and the relative IMFs were calculated.
- For each IMF the Pearson's linear correlation coefficient, ρ_P, with respect to the original signal was computed.
- IMFs with $\rho_P \geq 0.2$ were considered true features of the signal, whilst lower values were associated with background noise and/or fluctuations on the mean values. As shown in previous studies, greater correlation coefficients with the original signal lead to more important IMFs [55, 56]. No proper threshold value exists, but 0.2 is considered a good threshold to separate acoustic modes from generic turbulence noise [57].
- A new signal, $y(t)$, was generated by the summation of the IMFs with $\rho_P \geq 0.2$. This was then decomposed using VMD.

The analysis procedure used the strengths of both the EEMD and VMD algorithms. EEMD was used as an initial filter, followed by VMD, due to its greater ability to isolate single components.

The time spectral map (Fig. 7) indicated the complex nature of the events underlying the cavity's acoustic footprint. Although it was possible to distinguish an accumulation of energy in the band between 100 Hz to 1 kHz, strong deviations and local time features were present. The EEMD procedure determined twelve IMFs of which, as shown in Table 1, only five had a Pearson correlation coefficient above the defined threshold to be considered true features of the signal.

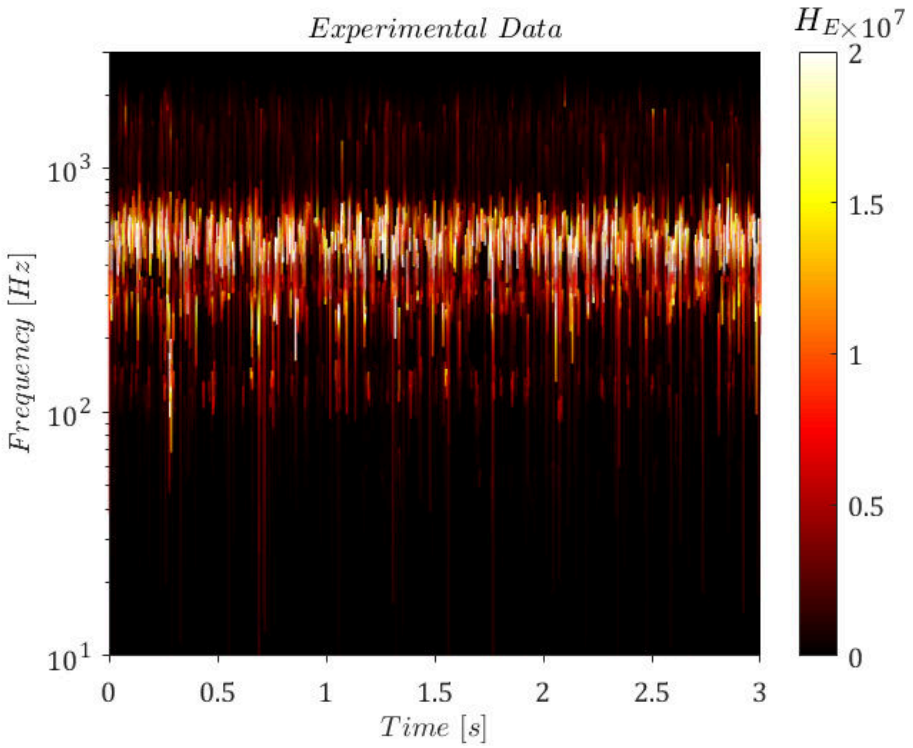

Figure 7: Hilbert spectral energy map for the pressure signal at $x/L = 0.95$, $2y/W = 0.50$, $z/D = 1.00$. Mach number 0.85. Experimental data from Henshaw [38], EEMD decomposition.

Table 1: Summary of the IOASPL and Pearson correlation coefficient (in decreasing order) for different intrinsic mode functions (IMFs) obtained with the EEMD decomposition method. Experimental data of Henshaw [38] extracted at $x/L = 0.95$, $2y/W = 0.50$, $z/D = 1.00$. Mach number 0.85.

IMF ID	IOASPL (dB)	ρ_P
2	160.9	0.8354
3	157.1	0.8127
4	154.3	0.4878
5	149.2	0.3134
6	145.7	0.2139
1, 7, 8, 9, 10, 11, 12	< 142.0	< 0.2000

To characterize the nature of each IMF, the marginal Hilbert spectrum was calculated (Fig. 8). A property of the marginal Hilbert spectrum is the fact that second order phenomena, such as IMF6 and IMF5, attained similar and/or higher $h(\omega)$ values compared to IMFs representing the Rossiter-

Heller tones. However, the marginal Hilbert spectrum is a statistical indicator. As such it does not indicate the energy associated in a frequency bin, rather the likelihood that in the temporal length of the signal a wave having a frequency corresponding to the bin under consideration would occur [52]. Hence, a non-linear and highly variable phenomenon, such as the Rossiter-Heller mode that is subjected to strong frequency modulation behavior, distributes energy over a wide frequency band. As an example, IMF6 had an associated IOASPL of 145 dB; 15 dB lower than IMF2. Nevertheless, whilst the former had a bandwidth of approximately 30 Hz, the latter had a bandwidth of over 400 Hz. Hence, IMF2 'spread' its associated energy over a bigger frequency interval, and the resulting maximum value of $h(\omega)$ was lower than that for IMF6.

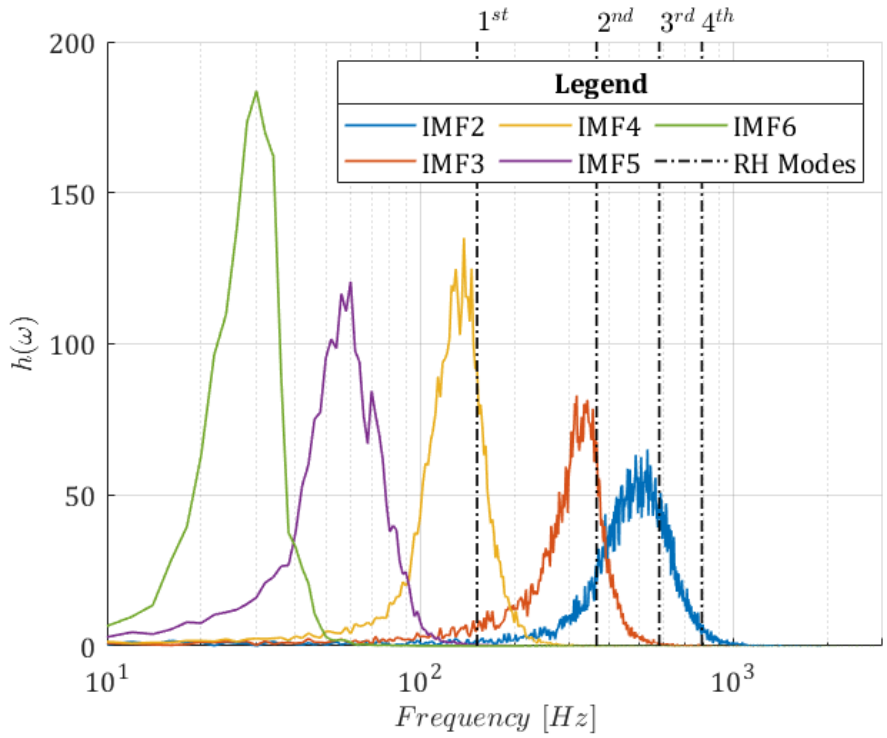

Figure 8: Marginal Hilbert spectrum of the principal IMFs (according to the classification in Table 1) for the pressure signal at $x/L = 0.95$, $2y/W = 0.50$, $z/D = 1.00$. Mach number 0.85. Experimental data from Henshaw [38], EEMD decomposition.

The analysis above indicated that each mode had a characteristic frequency band with a distinguishable peak and bandwidth. IMF6 correlated with the resonance mode associated with low-frequency modulation phenomena. This typically relates to the centrifugal and transverse instability [4–7]. The peak of IMF5, centered at 60 Hz according to Delprat's decomposition, is associated

with an amplitude modulation of the main resonant tones. Nevertheless, a corresponding peak for f_a was not present (for the experimental dataset, Delprat's decomposition indicated the following values: $f_a = 222$ Hz; $f_b = 81$ Hz; $\xi = 0.365$). The remaining IMFs (2, 3 and 4) were associated with the Rossiter-Heller tones.

Cavity flows exhibit AM and FM characteristics, as well as non-linear frequency coupling [4, 8, 9]. To investigate these characteristics a further decomposition, using the VMD procedure, was conducted. This used a signal obtained by the summation of the representative modes from the EEMD procedure and applied the strength of the VMD method, best suited to extract AM and FM features, even in closed-coupled conditions typical of cavity flows. The result of the decomposition was nine IMFs, representing several features of the flow. The marginal Hilbert spectrum (Fig. 9) showed the co-existence of several features.

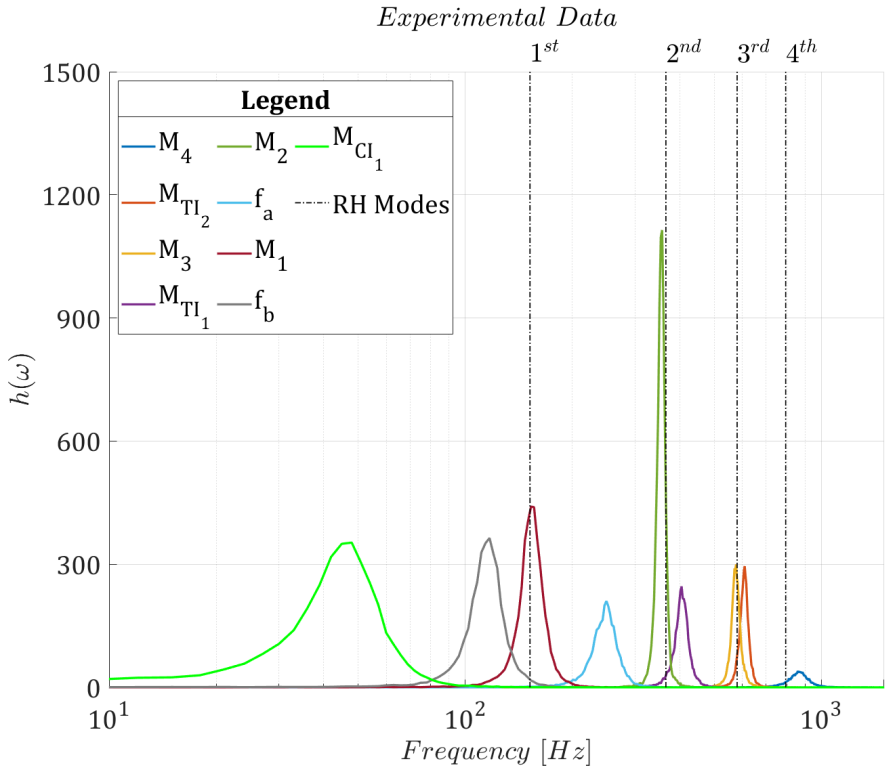

Figure 9: Marginal Hilbert spectrum of the pressure signal at $x/L = 0.95$, $2y/W = 0.50$, $z/D = 1.00$. Mach number 0.85. Experimental data from Henshaw [38], EEMD decomposition.

Four Rossiter-Heller modes were observed with the following IOASPL values: M_1 (155 dB at 153 Hz), M_2 (161 dB at 357 Hz), M_3 (155 dB at 576 Hz), and M_4 (147 dB at 858 Hz). SPL could not

reliably be used in this case because the modes extracted in the Hilbert spectrum have a FM behavior with the energy spread across a number of frequency bins, reducing the peak value. It was decided, therefore, that the IOASPL calculated for each mode was a better indicator of the associated acoustic power of each IMF. The spectrum also provided the Delprat fundamental acoustic frequency f_a (152 dB at 249 Hz) and amplitude modulation frequency f_b (154 dB at 117 Hz). The co-existence of these two frequencies with the Rossiter-Heller modes validated the dyadic nature of the cavity flow phenomena as well as its non-linear interaction, where the resonating shear layer (of which f_a represents the fundamental frequency) interacts with the centrifugal instabilities of the main recirculating vortex inside the cavity (of which f_b represents the fundamental frequency). An additional mode was observed, labelled M_{CI_1} in Fig. 9 and with an IOASPL of 152 dB at 48 Hz, representing a slow dynamic relative motion between the recirculating layers inside the cavity. The existence of multiple centrifugal instabilities was in line with other studies [7],

The two remaining peaks present in the marginal Hilbert spectrum (Fig. 9) were associated with transverse modes. Such instabilities are again correlated to the main recirculation inside the cavity, but in this case the resonating frequency was associated with oscillations in the transverse direction. The associated modes were labelled M_{TI_1} (153 dB at 406 Hz) and M_{TI_2} (154 dB at 609 Hz).

The analysis of the experimental data demonstrated the strength of the Hilbert-Huang spectral analysis with EEMD/VMD decomposition and its ability to properly identify the main flow features of a complex fluid-dynamic phenomenon associated with the aero-acoustics of cavity flows.

V. Results

The spectrum of an open-type cavity is typically characterized by three different components. The first is a broadband white noise, which may include peaks that are associated with centrifugal instability modes [5–7]. The second component typically comprises red noise, and contains the peaks associated with the Rossiter-Heller modes, which are typically the dominant tones in the spectrum. The third component has no prominent peaks and this background noise is again of the red type. This represents the turbulent decay, in the limits of the capacity of the turbulence model

to capture this phenomenon whenever the spectrum in computed after a CFD simulation.

The results are presented in two parts. First, a conventional Fourier analysis is presented, which shows the effect of the fluidic spoilers on the acoustic spectrum. Second, the Hilbert-Huang analysis is conducted on the numerical data sets, which leads to greater insight into the complex nature of the aero-acoustic behavior of the cavity flow.

A. The effect of fluidic spoilers on the acoustic spectrum

1. Mach 0.85

At Mach 0.85, Fourier analysis indicated that the fluidic spoilers reduced considerably the overall presence of the Rossiter-Heller modes, influencing all the significant areas of the cavity spectrum. Fig. 10 presents the acoustic spectra and shows that, with $C_\mu = 0.03$, M_1 was reduced by 8 dB, M_2 by 3 dB, and M_3 was reduced to near broadband noise levels, experiencing a drop of 12 dB. Excitation at lower frequencies was reduced as well, by an average of 11 dB. The frequency of the tones in the spectrum remained unchanged with respect to the reference case ($C_\mu = 0.0$). The result confirmed the beneficial effect of the fluidic spoiler, and flow visualization showed how the reduction was a direct consequence of two effects induced by the mass flow injection: 1. a deflection of the shear layer away from the cavity entrance (Fig. 11); 2. a splitting of the onset boundary layer flow into smaller vortical structures (Fig. 12). The latter aspect is particularly relevant to cavity noise suppression, since reducing the coherence of the detached eddies reduces significantly the energy impinging on the cavity trailing edge, and the subsequent acoustic emissions. Fig. 13 shows the effect of the fluidic spoilers on the shear layer position near the cavity leading edge. The minimum value of the Reynolds stress term, $\overline{\rho uu}$, close to $z/D = 0$ provides a good indication of the shear layer position. With the spoilers switched off the shear layer is at $z/D = -0.12$, moving to $z/D = -0.056$ with $C_\mu = 0.03$, and $z/D = -0.043$ with $C_\mu = 0.06$.

Previous CFD studies on saw-tooth type spoilers [58–60] demonstrated that a similar splitting of the shear layer into smaller structures occurred as well. The experimental study of Singh et al. [27], which used passive leading-edge tabs, supported the conclusions of the CFD studies. Furthermore,

it demonstrated the same flow-changing phenomena as experiments using fluidic actuators, for example Lusk et al. [18]. Since saw-tooth spoilers are a well know passive method by which the acoustic noise can be reduced [11], it is reasonable to assume that fluidic spoilers of the type used in the current study achieve palliative effects based on a similar induced effect on the flow.

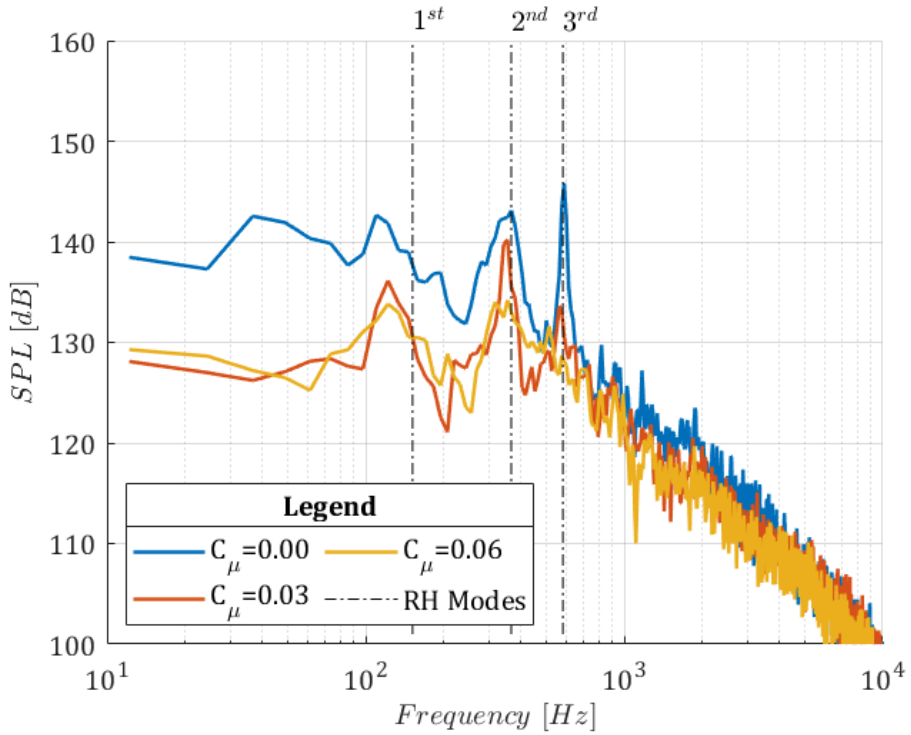

Figure 10: The effect of the fluidic spoilers on the spectrum of the pressure signal at $x/L = 0.95$, $2y/W = 0.50$, $z/D = 1.00$, $M = 0.85$; v2w000 geometry.

Increasing C_μ to 0.06 further decreased the SPL of the resonant modes as a consequence of a greater deflection and breakup of the cavity shear layer. M_3 was completely suppressed, whilst M_1 and M_2 were reduced by a further 2 dB and 6 dB respectively (Fig. 10). No appreciable reduction of the broadband noise and the low frequency band power was observed, however, which means that there was only 1.2 dB difference in the OASPL levels (determined from the SPL data) between the two blowing coefficients at $x/L = 0.95$.

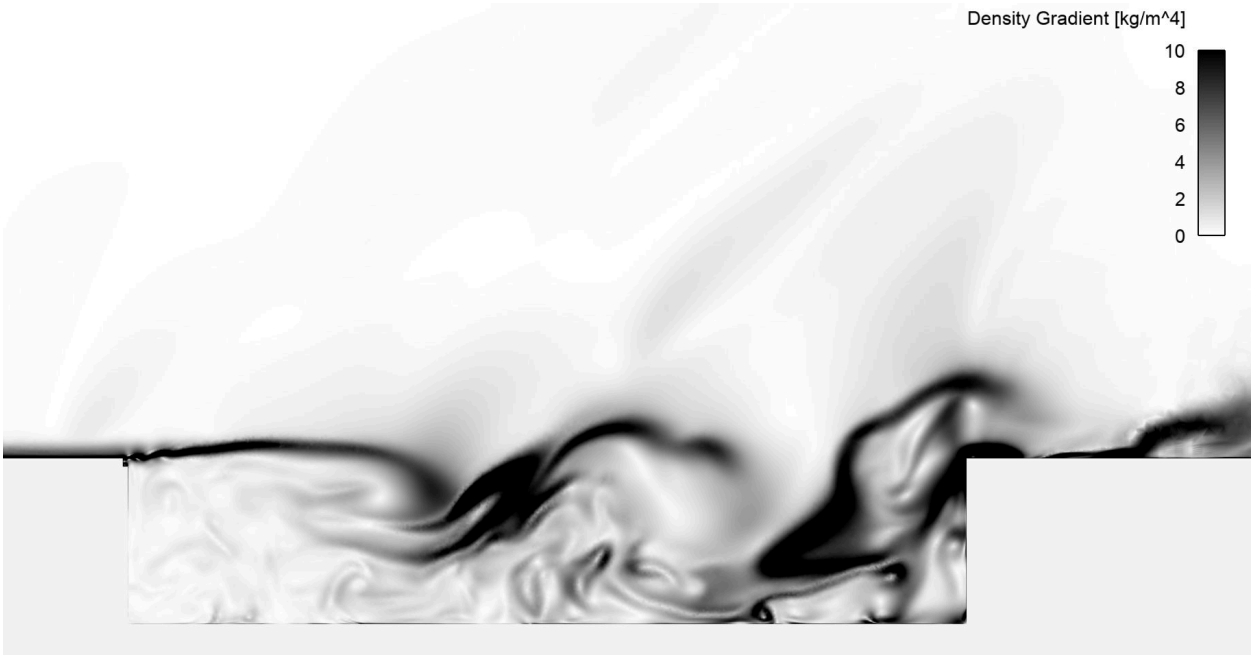

(a) $C_\mu = 0.00$

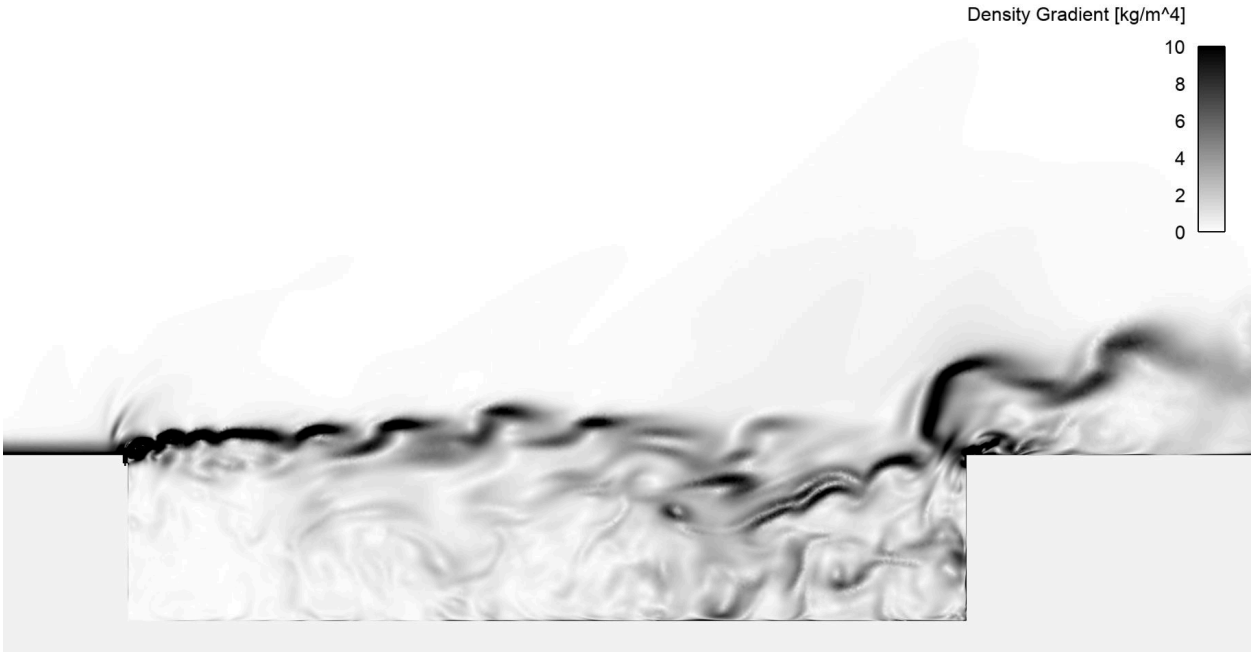

(b) $C_\mu = 0.03$

Figure 11: The effect of the fluidic spoilers on the cavity flow eddy structures showing how spoiler operation reduced the coherence of the shear layer and diverted it away from the cavity entrance. Contours of density gradient at $2y/W = 0.00$, $M = 0.85$; v2w000 geometry

2. Mach 1.2

At a freestream Mach number of 1.2 the acoustic spectrum of the cavity with $C_\mu = 0$ was characterized by three dominant peaks, corresponding to the Rossiter-Heller modes M_2, M_3 and M_4

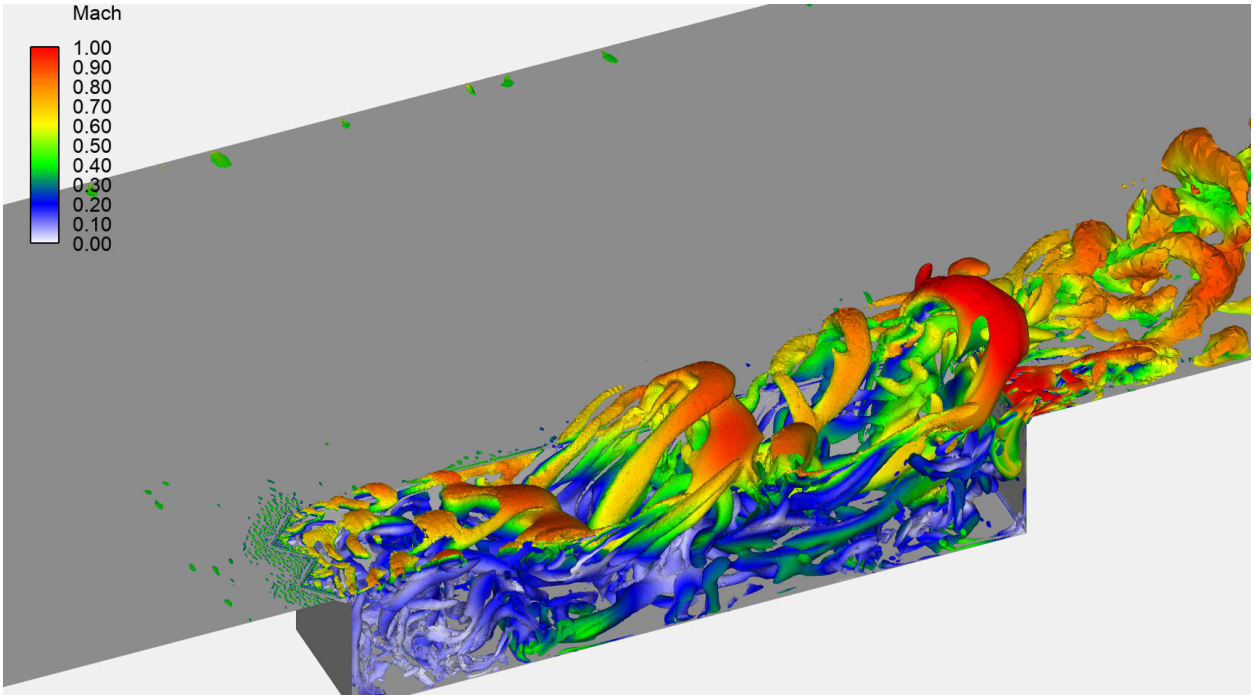

(a) $C_\mu = 0.00$

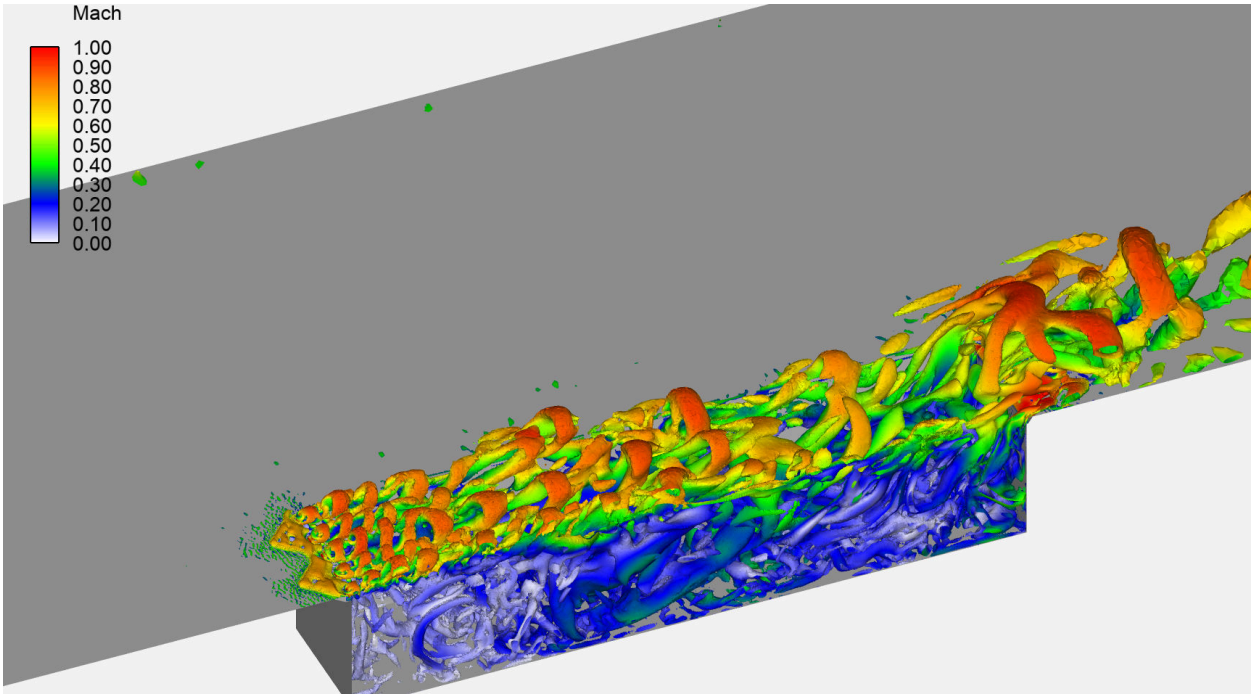

(b) $C_\mu = 0.03$

Figure 12: The effect of the fluidic spoilers on the cavity flow vortical structures (represented by the isosurface of Q-criterion colored by Mach number) showing how spoiler operation reduced the coherence of the shear layer. Flow from left to right. $M = 0.85$; v2w000 geometry

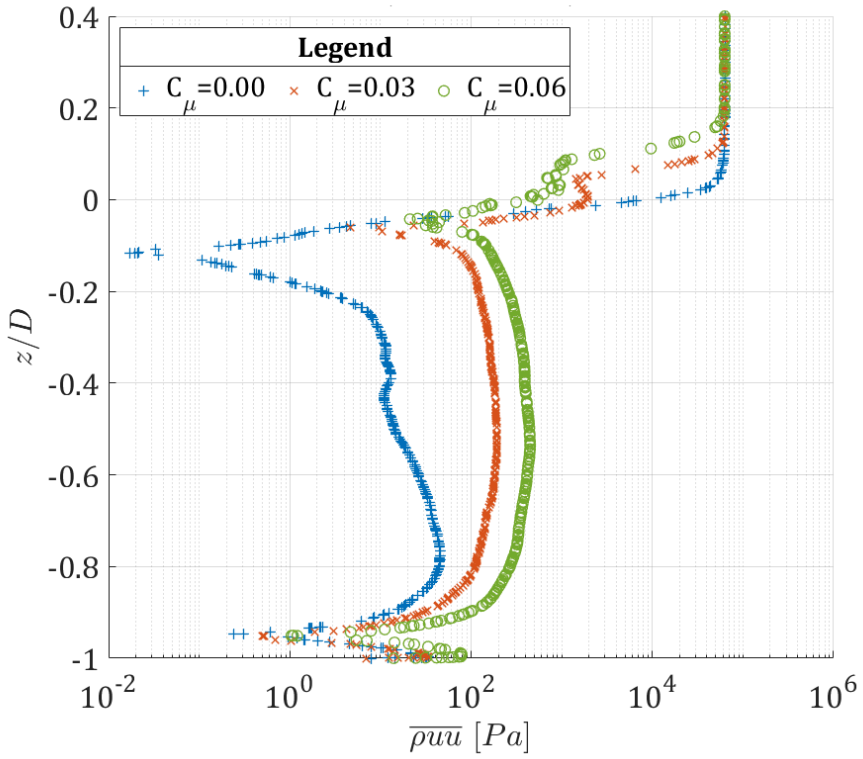

Figure 13: The effect of the fluidic spoilers on the shear layer position (indicated by the minimum value of the Reynolds stress term near $z/D = 0$) near the cavity leading edge at $x/L = 0.05$, $2y/W = 0.50$, $M = 0.85$; v2w000 geometry.

(Fig. 14). A fourth mode, which could be associated with the first Rossiter-Heller tone, was located at a frequency different to the theoretically-predicted value. The four modes had the following properties: M_1 (140 dB at 130 Hz); M_2 (151 dB at 439 Hz); M_3 (146 dB at 716 Hz); M_4 (139 dB at 993 Hz). An additional mode was located at 277 Hz, with a power of 140 dB. According to Delprat's decomposition this peak was associated with the fundamental frequency, f_a.

The fluidic spoilers, with $C_\mu = 0.03$, improved the tonal noise. M_4 was eliminated, whilst the M_2 and M_3 spectral power was reduced by 9 dB. The SPL of M_1 also dropped (by 5 dB). The mode frequency was changed as well, from the previous value of 130 Hz to 179 Hz. Finally, the high-frequency broadband noise was reduced by 3 dB, whilst the low-frequency spectral content experienced an average drop of 9 dB. A further increase in C_μ eliminated M_3. M_2 was reduced to 134 dB (-8 dB with respect to $C_\mu = 0.03$), almost to the level of the background noise. The broadband noise at low and high frequencies was further reduced by 1 dB, however M_1 did not

experience a reduction.

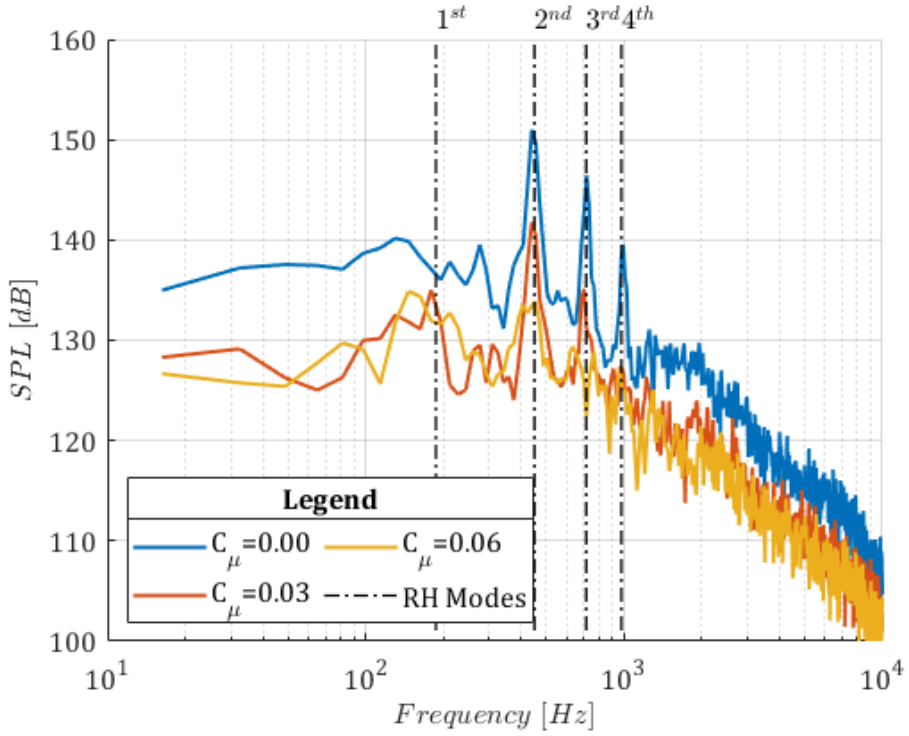

Figure 14: Effect of the fluidic spoilers on the spectrum of the pressure signal at $x/L = 0.95$, $2y/W = 0.50$, $z/D = 1.00$, $M = 1.2$; v2w000 geometry.

3. Mach 1.8

Increasing the freestream Mach number to 1.8 resulted in a spectrum with multiple peaks. Fourier spectral analysis showed the presence of six Rossiter-Heller modes, of which the 5th had the highest amplitude (Fig. 15). This trend was in line with other studies on similar cavities [60, 61]. The resonant modes had the following characteristics: M_1 (131 dB at 183 Hz); M_2 (137 dB at 586 Hz); M_3 (134 dB at 964 Hz); M_4 (141 dB at 1318 Hz); M_5 (143 dB at 1648 Hz); M_6 (131 dB at 1953 Hz). Similar to the Mach 1.2 case, a peak corresponding to the fundamental frequency, f_a (130 dB at 354 Hz), was present in the spectrum. Activation of the fluidic spoilers completely suppressed all resonant modes. This was observed for both blowing coefficients, with minimal difference between the two settings. In both cases ($C_\mu = 0.03$ and $C_\mu = 0.06$) only M_1 was still identifiable in the spectrum, whilst all other modes were reduced to broadband noise, with an SPL of 125 dB. High

and low frequency spectral content also experienced a decrease in noise levels with an average reduction, with respect to $C_\mu = 0$, of 7 dB for the former and 8 dB for the latter.

It is notable that there is a distinct change in the number of acoustic tones and their relative amplitude as Mach number increases from 0.85, through Mach 1.2, to Mach 1.8. The increase in the number of resonating tones with Mach number is believed to be related to the presence of the cavity's leading edge oblique shock wave. As Mach number increases the shock is inclined towards the cavity and its trailing edge. Further research would be needed to investigate and explain this behavior.

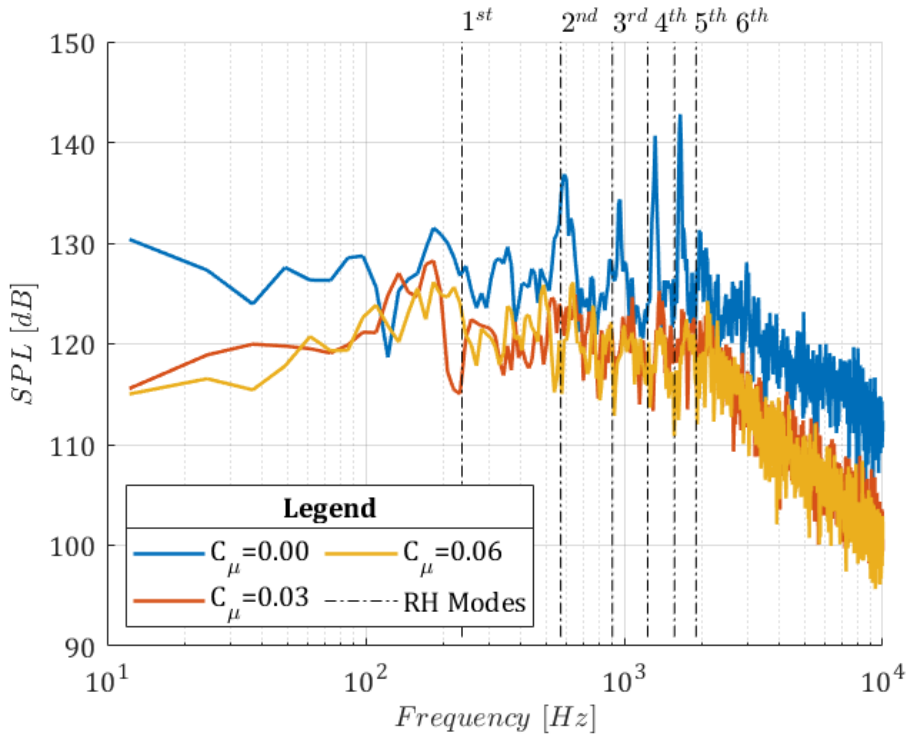

Figure 15: Effect of the fluidic spoilers on the spectrum of the pressure signal at $x/L = 0.95$, $2y/W = 0.50$, $z/D = 1.00$, $M = 1.8$; v2w000 geometry.

B. Hilbert-Huang time-spectral analysis of fluidic spoiler effects

The Hilbert-Huang analysis procedure was applied to the numerical simulation in order to obtain a deeper understanding of the effect of fluidic spoilers on cavity flow structures at transonic and supersonic speeds.

1. Mach 0.85

Fig. 16 shows the marginal Hilbert spectrum of the transonic case (Mach 0.85) with spoilers off and identified the existence of four Rossiter-Heller modes: M_1 (157 dB at 148 Hz), M_2 (162 dB at 340 Hz), M_3 (160 dB at 580 Hz), and M_4 (149 dB at 896 Hz). The result was in disagreement with the spectral analysis (Fig. 10) where only three Rossiter-Heller modes were observed and where the power associated with M_3 was greater than that associated with M_2. The Hilbert spectral analysis indicated, however, that these two resonant modes had similar amplitudes. This fact is explained by the FM nature of the modes in this configuration, as the time spectral map (Fig. 17) clearly shows, where the nature of the modes was strongly intermittent, with periods of activity separated by a complete disappearance of acoustic modes.

Fig. 17 (label 1) indicates the point where, at approximately 0.22 s, the Hilbert spectral energy suddenly increases following approximately 0.02 s of inactivity. Additionally, during the temporal evolution of the signal, the frequencies associated with the modes varied in time (Fig. 17, label 2), often randomly. This caused a distribution of the energy associated with each mode across a wider frequency band, instead of being concentrated in a narrow frequency bin, leading to a distortion of the outcome of the Fourier analysis of the signal.

Further inspection of the marginal Hilbert spectrum (Fig. 16) identified a tone associated with the transverse instability, M_{TI_1} (149 dB at 694 Hz), a centrifugal instability mode, with strong FM behavior, M_{CI_1} (159 dB at 48 Hz), and Delprat's amplitude modulation frequency f_b (154 dB at 126 Hz). Interestingly, no peak was observed in the band typically associated with the fundamental acoustic tone of the cavity, f_a, contrary to the M219 case (Fig. 9). The reason for this is the difference in geometry between the two test cases.

Activation of the fluidic spoilers changed the characteristic of the flow considerably. The marginal Hilbert spectrum (Fig. 16) indicated the presence of two Rossiter-Heller modes: M_2 (156 dB at 350 Hz), M_3 (151 dB at 546 Hz), the transverse instability mode M_{TI_1} (149 dB at 670 Hz) and Delprat's modulating frequency (or centrifugal instability) f_b (153 dB at 120 Hz). Noticeably, the low-frequency instability mode, present with the fluidic spoilers turned off ($C_\mu = 0$), completely disappeared, as well as the peak corresponding to the first Rossiter-Heller tone. In line

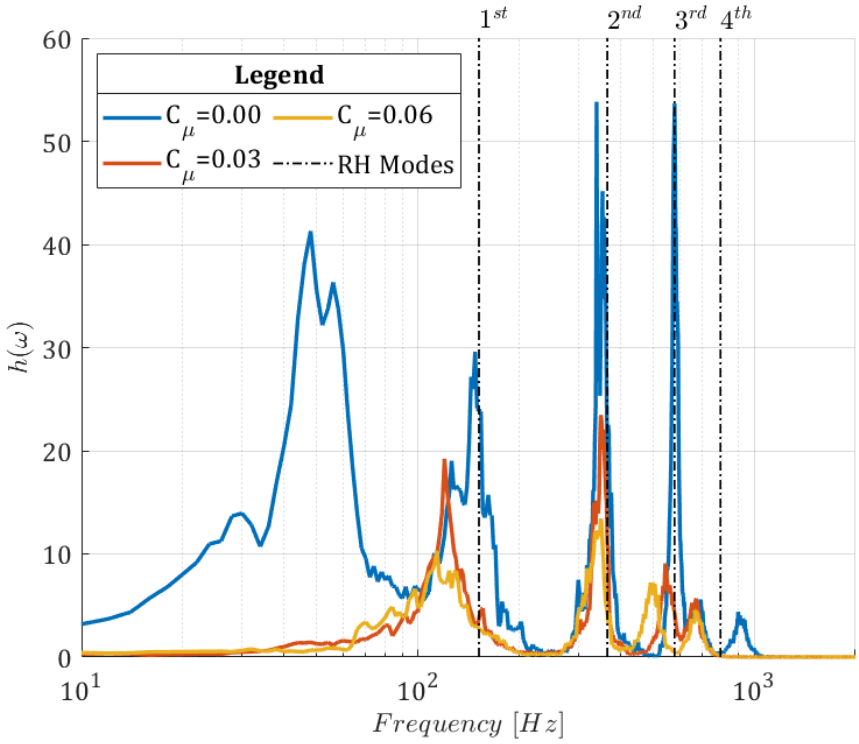

Figure 16: The effect of fluidic spoilers on the marginal Hilbert spectrum of the pressure signal at $x/L = 0.95, 2y/W = 0.50, z/D = 1.00, M = 0.85$. EEMD+VMD decomposition; v2w000 geometry.

with the Fourier analysis (Fig. 10), M_4 was eliminated and the remaining modes experienced a substantial reduction of the allocated power. The three regions indicated by label 3 in Fig. 17 highlight examples where this was also observed in the time-frequency map.

The Hilbert-Huang analysis was able to identify two features not discernible from the basic Fourier analysis. The first, as already described, was the disappearance of M_{CI_1}. The activation of the fluidic spoilers changed the internal flow recirculation structure. From the two eddy arrangement with $C_\mu = 0$, a new system characterized by a single vortex was established. This reduced the number of sources for the centrifugal instability, and rather than the previous two observed modes (M_{CI_1} and f_b), now only the one associated with the main eddy structure appeared (f_b). The second prominent change in the Hilbert spectrum (Fig. 16) was the disappearance of M_1. A hypothesis for the cause of this was a lifting of the shear layer. The existence of the second and third Rossiter-Heller tones confirmed that the interaction between the shear layer and the main cavity eddy was still active, however, M_1 had a wavelength of the order of four times the cavity length, implying

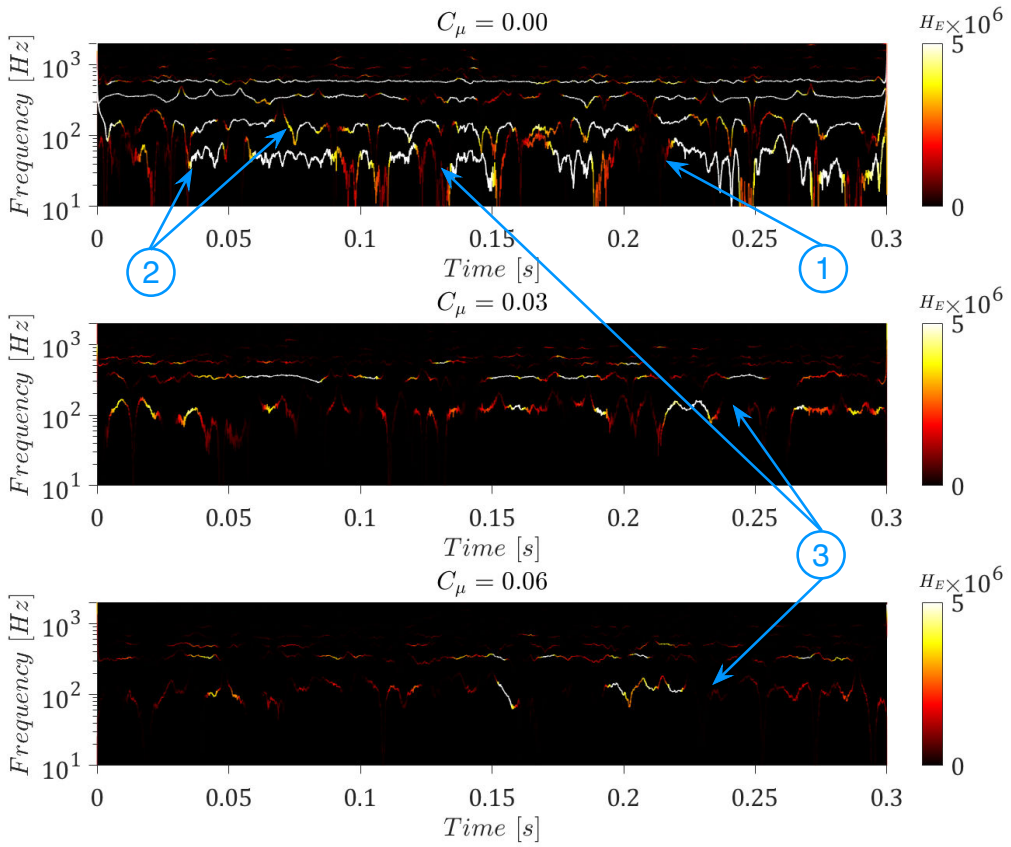

Figure 17: The effect of fluidic spoilers on the Hilbert spectral energy of the pressure signal at $x/L = 0.95, 2y/W = 0.50, z/D = 1.00, M = 0.85$. EEMD+VMD decomposition; v2w000 geometry.

that the relative node-antinode distance was greater than the cavity longitudinal dimension. In such a condition, a lifting of the shear layer should make the appearance of M_1 impossible.

A higher blowing coefficient ($C_\mu = 0.06$), introduced two main differences with respect to the $C_\mu = 0.03$ case. Firstly, the power levels of M_2 and f_b were reduced, by 2.8 dB and 1.2 dB respectively. Secondly, M_3, apart from reducing its IOASPL by 1 dB, experienced a frequency change in the location of its peak, from the previous 546 Hz to 492 Hz, but no direct explanation was found for this. Finally, the transverse instability mode, M_{TI_1} remained unchanged.

2. *Mach 1.2*

Fig. 18 shows that with the fluidic spoilers off the cavity presented four peaks: M_1 (154 dB at 180 Hz); M_2 (167 dB at 440 Hz); M_3 (163 dB at 715 Hz); M_4 (157 dB at 980 Hz). In contrast to the high

subsonic Mach number case, the marginal Hilbert spectrum at $M = 1.20$ presented peaks only at the associated Rossiter-Heller frequencies, which is in agreement with the standard spectral analysis (Fig. 14). No additional modes appeared, indicating that the transition from a high subsonic to supersonic flow regime altered the non-linear interaction between the dominant fluid structures inside the cavity, making the Rossiter-Heller modes dominant. This is in agreement with previous studies [62, 63].

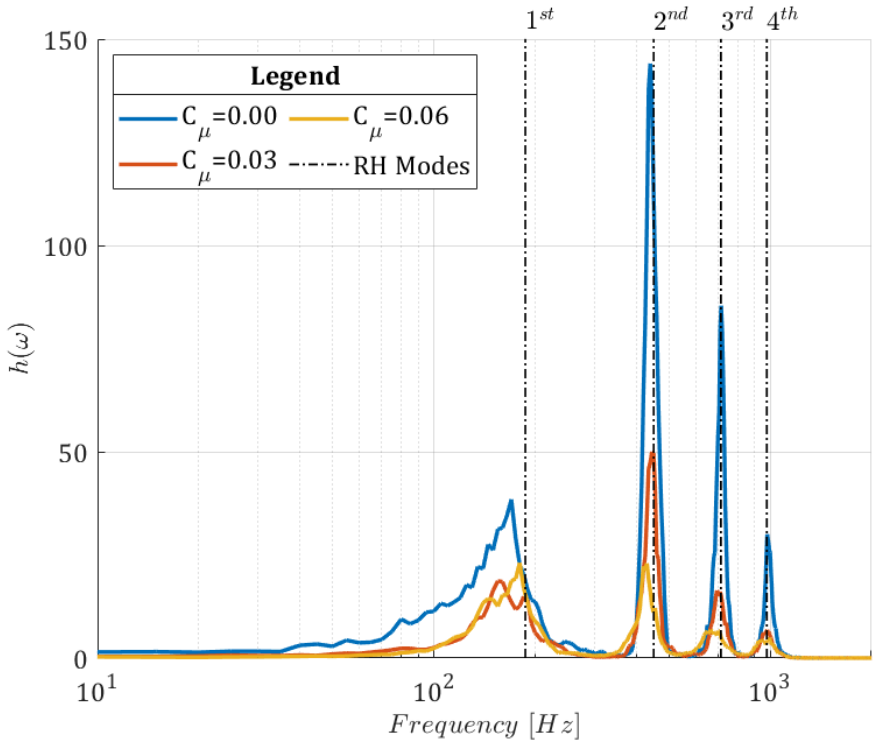

Figure 18: The effect of fluidic spoilers on the marginal Hilbert spectral energy of the pressure signal at $x/L = 0.95$, $2y/W = 0.50$, $z/D = 1.00$, $M = 1.20$. EEMD+VMD decomposition; v2w000 geometry.

Operating the fluidic spoilers did not change the qualitative aspect of the spectrum (Fig. 18), but it did reduce the acoustic level of the modes. The IOASPL reductions (with respect to the spoilers switched off) observed through the Hilbert spectral analysis were for M_2 -8.6 dB ($C_\mu = 0.03$) and -13.0 dB ($C_\mu = 0.06$), for M_3 -10.1 dB ($C_\mu = 0.03$) and -12.9 dB ($C_\mu = 0.06$), and for M_4 -8.5 dB ($C_\mu = 0.03$) and -9.3 dB ($C_\mu = 0.06$). Finally, whilst the IOASPL for M_1 was reduced by 7.1 dB, when the blowing coefficient was 0.03, at $C_\mu = 0.06$ the reduction was only 6.8 dB.

3. Mach 1.8

Fig. 19 shows the marginal Hilbert spectrum for $M = 1.80$, which is qualitatively the same as the Fourier analysis (Fig. 15), with the presence of multiple peaks dominated by the 5th Rossiter-Heller mode. However, the Hilbert-Huang analysis identified seven Rossiter Heller modes, and the presence of the fundamental acoustic frequency f_a was also observed. Regarding the Rossiter-Heller modes, the following data was extracted: M_1 (153 dB at 234 Hz); M_2 (157 dB at 569 Hz); M_3 (154 dB at 960 Hz); M_4 (159 dB at 1308 Hz); M_5 (161 dB at 1656 Hz); M_6 (154 dB at 1956 Hz); M_7 (150 dB at 2208 Hz). Finally, f_a had a power of 151 dB and a central frequency of 312 Hz. The calculated modes where in line with the theoretically-predicted values. As in the $M = 1.20$ case, the modulating frequency, f_b did not appear in the Hilbert spectrum, however f_a was present.

Although analysis of the mean flow did not provide evidence of any change in the characteristics of the internal flow structure inside the cavity, the activation of the spoilers altered significantly the location of the modes. Applying Delprat's decomposition [4] to the reference configuration ($C_\mu = 0$) the values of $f_a = 329$ Hz and $f_b = 45$ Hz were obtained. For $C_\mu = 0.03$ the values were $f_a = 380$ Hz and $f_b = 163$ Hz, whilst for $C_\mu = 0.06$, $f_a = 357$ Hz and $f_b = 111$ Hz were obtained.

From the manipulation of Eqn. 2, it was possible to determine an expression relating the difference between the central frequencies of a Rossiter-Heller mode, of two different cases (1 and 2), subjected to different values of f_a and f_b.

$$f_{n_2} = f_{n_1} + n \cdot \Delta f_a - \Delta f_b \tag{17}$$

where,

$$\Delta f_a = f_{a_2} - f_{a_1} \tag{18}$$

$$\Delta f_b = f_{b_2} - f_{b_1} \tag{19}$$

Applying these relations to the values extracted from the marginal Hilbert spectrum shown in

Fig. 19, it was observed that the relationship described in Eqn. 17 was satisfied in all cases with a maximum error of ± 5 Hz, which was of the order of the frequency resolution adopted in the Hilbert-Huang spectral analysis. This finding confirmed that when the spoilers were activated the changes observed in the Hilbert spectrum were a direct and sole consequence of the change in the fundamental acoustic frequency f_a and the centrifugal instability mode f_b.

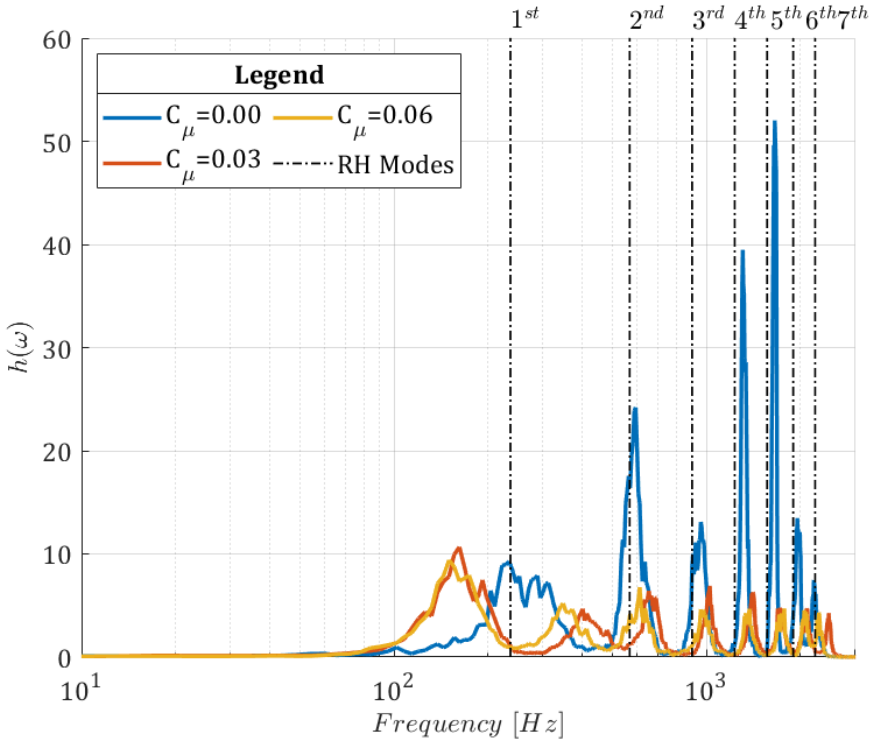

Figure 19: The effect of fluidic spoilers on the marginal Hilbert spectral energy of the pressure signal at $x/L = 0.95$, $2y/W = 0.50$, $z/D = 1.00$, $M = 1.80$. EEMD+VMD decomposition; v2w000 geometry.

The spoilers considerably reduced the IOASPL associated with each mode but the amount of acoustic noise reduction was different for each mode. Irrespective of the original IOASPL that each tone had in the reference case, when the spoilers were activated the overall acoustic level of all modes were reduced to below 149 dB for $C_\mu = 0.03$, and below 147.5 dB for $C_\mu = 0.06$.

VI. Conclusions

The study confirmed that fluidic spoilers, located at the leading-edge step of a low-RCS geometry, were capable of reducing the acoustic noise levels comparable to that observed in similar spoiler geometries applied to basic rectangular cavities. The numerical computations indicated that the palliative mechanism maintained its performance for Mach numbers ranging from subsonic to supersonic. The blowing coefficients needed to reduce acoustic tones was in line with the findings of previous studies, and the existence of a plateau in the value of C_μ, above which no further benefits are observed, was confirmed as well.

Spectral analysis confirmed the palliative capabilities of the fluidic spoilers, which considerably reduced, and often suppressed, all the resonant modes at all Mach numbers. In the Mach 0.85 case, the Rossiter-Heller modes' SPL reduction was up to 9 dB, whilst low frequency noise levels were lowered by 11 dB. At supersonic Mach numbers, activation of the spoilers reduced the first Rossiter-Heller tone (M_1) by 5 dB, whilst the second mode, M_2 was reduced by up to 17 dB at Mach 1.20 and completely suppressed at Mach 1.80. At both supersonic speed regimes low and high broadband frequency noise reduction was as high as 10 dB.

Flow visualization indicated that the fluidic spoilers palliative effect was achieved by inducing flow modifications similar to those introduced by saw-tooth spoilers. In fact, air blown from the slots had the double effect of diverting the shear layer away from the cavity, and splitting it into smaller and less-coherent structures, that upon impact at the trailing edge resulted in less radiated acoustic noise and in a less coordinated feedback-loop. The former effect was in general responsible for a lowering of the noise level, especially at low frequency, and the latter was associated with a disruption of the Rossiter-Heller tones.

The Hilbert-Huang spectral analysis provided an enhanced understanding of the complex nature of the aero-acoustic behavior of the cavity. Acoustic modes were identified that, together with the Rossiter-Heller tones, govern the behavior of the spectrum. This demonstrated how the generated tones, appearing inside the cavity, were a result of complex non-linear interactions between shear layer acoustic instabilities and centrifugal instabilities originating in the flow recirculating in the

internal part of the cavity. This also demonstrated that the fundamental frequencies had frequency and amplitude modulation characteristics that spread the energy in a wide bandwidth. This is not captured by classical Fourier analysis.

References

[1] D. Rockwell and E. Naudasher. Review – self sustaining oscillations of flow past cavities. *Journal of Fluids Engineering*, 100(2):152–165, 1978. doi: 10.1115/1.3448624.

[2] J. E. Rossiter. Wind-tunnel experiments on the flow over rectangular cavities at subsonic and transonic speeds. Reports and Memoranda 3438, Aeronautical Research Council, 1966.

[3] H. Heller, D. Holmes, and E. Covert. Flow-induced pressure oscillations in shallow cavities. *Journal of Sound and Vibration*, 18:545–553, 1971. doi: 10.1016/0022-460X(71)90105-2.

[4] N. Delprat. Low-frequency components and modulation processes in compressible cavity flows. *Journal of Sound and Vibration*, 329(22):4797–4809, 2010. doi: 10.1016/j.jsv.2010.05.013.

[5] G. A. Brès and T. Colonius. Three-dimensional instabilities in compressible flow over open cavities. *Journal of Fluid Mechanics*, 599:309–339, 2008. doi: 10.1017/S0022112007009925.

[6] L. Larchevêque, P. Sagaut, T.-H. Lê, and P. Comte. Large-eddy simulation of a compressible flow in a three-dimensional open cavity at high Reynolds number. *Journal of Fluid Mechanics*, 516:265–301, 2004. doi: 10.1017/S0022112004000709.

[7] J. Basley, L. R. Pastur, F. Lusseyran, J. Soria, and N. Delprat. On the modulating effect of three-dimensional instabilities in open cavity flows. *Journal of Fluid Mechanics*, 759:546–578, 2014. doi: 10.1017/jfm.2014.576.

[8] M. A. Kegerise, E. F. Spina, S. Garg, and L. N. Cattafesta. Mode-switching and nonlinear effects in compressible flow over a cavity. *Physics of Fluids*, 16(3):678–687, 2004. doi: 10.1063/1.1643736.

[9] D. Bacci, A. J. Saddington, and D. Bray. Identification of the formation of resonant tones in compressible cavity flows. *Aerospace Science and Technology*, 77:320–331, 2018. doi: 10.1016/j.ast.2018.03.013.

[10] L. Mongeau, H. Kook, and M. Franchek. Active control of flow-induced cavity resonance. In *4th AIAA/CEAS Aeroacoustics Conference*, number 1998-2349, Toulouse, France, 2-4 June 1998. doi: 10.2514/6.1998-2349.

[11] V. Thangamani, K. Knowles, and A. J. Saddington. The effects of scaling on high subsonic cavity flow oscillations and control. *Journal of Aircraft*, 51(2):424–433, 2014. doi: 10.2514/1.C032032.

[12] A. J. Saddington, K. Knowles, and V. Thangamani. Scale effects on the performance of sawtooth spoilers in transonic rectangular cavity flow. *Experiments in Fluids*, 57(1):2:1–2:12, 2016. doi: 10.1007/s00348-015-2088-2.

[13] A. J. Saddington, V. Thangamani, and K. Knowles. Comparison of passive control methods for a rectangular cavity in transonic flow. *Journal of Aircraft*, 53(5):1439–1447, 2016. doi: 10.2514/1.C033365.

[14] Y. Zhang, Y. Sun, N. Arora, L. N. Cattafesta, K. Taira, and L. S. Ukeiley. Suppression of cavity flow oscillations via three-dimensional steady blowing. *AIAA Journal*, 57(1):90–105, 2019. doi: 10.2514/1.J057012.

[15] D. Sahoo, A. Annaswamy, N. Zhuang, and F. Alvi. Control of cavity tones in supersonic flow. In *43rd AIAA Aerospace Sciences Meeting and Exhibit*, number 2005-0793, Reno, NV, 10-13 January 2005.

[16] Y. Lee, M. Kang, H. Kim, and T. Setoguchi. Passive control techniques to alleviate supersonic cavity flow oscillation. *Journal of Propulsion and Power*, 24(4):697–703, 2008. doi: 10.2514/1.30292.

[17] N. Vikramaditya and J. Kurian. Pressure oscillations from cavities with ramp. *AIAA Journal*, 47 (12):2974–2984, 2009. doi: 10.2514/1.43068.

[18] T. Lusk, L. N. Cattafesta, and L. S. Ukeiley. Leading edge slot blowing on an open cavity in supersonic flow. *Experiments in Fluids*, 53:187–199, 2012. doi: 10.1007/s00348-012-1282-8.

[19] V. Thangamani and J. Kurian. Control of cavity oscillations in a supersonic flow by microjet injection. *Journal of Aircraft*, 50(4):1305–1309, 2013. doi: 10.2514/1.C032003.

[20] D. Roberts, D. MacManus, R. Johnson, J. Grove, T. Birch, and R. Chaplin. Passive attenuation of modal cavity aeroacoustics under supersonic and transonic conditions. *AIAA Journal*, 53(7): 1861–1877, 2015. doi: 10.2514/1.J053564.

[21] N. Webb and M. Samimy. Control of supersonic cavity flow using plasma actuators. *AIAA Journal*, 55(10):3346–3355, 2017. doi: 10.2514/1.J055720.

[22] K. Luo, W. Zhu, Z. Xiao, Z. Weng, L. Deng, D. Yang, and J. Liu. Investigation of spectral characterisitics by passive control methods past a supersonic cavity. *AIAA Journal*, 56(7):2669–2686, 2018. doi: 10.2514/1.J056689.

[23] X. Wang, D. Yang, J. Liu, and F. Zhou. Control of pressure oscillations induced by supersonic cavity flow. *AIAA Journal*, 58(5):2070–2077, 2020.

[24] A. M. Turpin, D. Chin, and K. Granlund. upersonic cavity flow subjected to continuous and transient leading-edge blowing. *AIAA Journal*, 58(10):4415–4425, 2020. doi: 10.2514/1.J059267.

[25] Q. Liu and F. Gómez. Role of trailing-edge geometry in open cavity flow control. *AIAA Journal*, 57(2):876–878, 2019. doi: 10.2514/1.J056977.

[26] Z. Liu, F. Ning, Q. Zhai, J. Wei, and B. Li. Study on oscillation phenomena in morphing cavities with ramps of leading wall. *Journal of Aircraft*, 58(3):436–447, 2021. doi: 10.2514/1.C035993.

[27] S. Singh, L. Ukeiley, Y. Zhang, L. N. Cattafesta, and K. Taira. Supersonic cavity flow control using a spanwise array of leading-edge tabs. *Journal of Aircraft*, 59(3):788–798, 2022. doi: 10.2514/1.C036678.

[28] L. Shaw. Active control for cavity acoustics. In *4th AIAA/CEAS Aeroacoustics Conference*, number 1998-2347, Toulouse, France, 2-4 June 1998.

[29] L. Shaw and S. Northcraft. Closed loop active control for cavity acoustics. In *5th AIAA/CEAS Aeroacoustics Conference*, number 1999-1902, Bellevue, WA, 10-12 May 1999.

[30] L. N. Cattafesta, Q. Song, D. R. Williams, C. L. Rowley, and F. S. Alvi. Active control of flow-induced cavity oscillations. *Progress in Aerospace Sciences*, 44(7-8):479–502, 2008. doi: 10.1016/j.paerosci.2008.07.002.

[31] J. M. Mendoza and K. K. Ahuja. Cavity noise control through upstream mass injection from a Coanda surface. In *AIAA and CEAS Aeroacoustics Conference*, number 96-1767, State College, PA, 6-8 May 1996.

[32] L. S. Ukeiley, M. Sheehan, F. Coiffet, F. Alvi, S. Arunajatesan, and B. Jansen. Control of pressure loads in geometrically complex cavities. *Journal of Aircraft*, 45(3):1014–1024, May-June 2008. doi: 10.2514/1.33324.

[33] G. J. Bennett, P. N. Zhao, K. Philo, Y. Guan, and S. C. Morris. Cavity resonance suppression using fluidic spoilers. *AIAA Journal*, 57(2):706–719, 2019. doi: 10.2514/1.J057407.

[34] P. A. Kreth and F. S. Alvi. Using high-frequency pulsed supersonic microjets to control resonant high-speed cavity flows. *AIAA Journal*, 58(8):3378–3392, 2020. doi: 10.2514/1.J058912.

[35] K. M. Casper, J. L. Wagner, S. J. Baresh, J. F. Henfling, R. W. Spillers, and B. O. M. Pruett. Complex geometry effects on cavity resonance. *AIAA Journal*, 54(1):320–330, 2016. doi: 10.2514/1.J054273.

[36] D. Bacci, A. J. Saddington, and D. Bray. Wavelet analysis of complex geometry transonic cavity flows. In *34th AIAA Applied Aerodynamics Conference*, number 2016-3177, Washington DC, USA, 13-17 June 2016.

[37] C. Kannepalli, C. Chartrand, R. Birkbeck, N. Sinha, and N. Murray. Computational modelling of geometrically complex weapons bays. In *17th AIAA/CEAS Aeroacoustics Conference*, number AIAA-2011-2774, Portland, OR, 5-8 June 2011.

[38] M. J. de C. Henshaw. M219 cavity case. In *Verification and validation data for computational unsteady aerodynamics*, number RTO-TR-26, AC/323(AVT)TP/19, pages 453–472. NATO, 2002.

[39] G. J. M. Loupy, G. N. Barakos, and N. J. Taylor. Cavity flow over a transonic weapons bay during door operation. *Journal of Aircraft*, 55(1):339–354, 2017. doi: 10.2514/1.C034344.

[40] D. Bacci, A. J. Saddington, and D. Bray. The effect of angle of attack on the aeroacoustic environment within the weapons bay of a generic UCAV. *Aerospace Science and Technology*, 93:105315(1–14), October 2019. doi: 10.1016/j.ast.2019.105315.

[41] Y. Sun, Q. Liu, L. N. Cattafesta, L. S. Ukeiley, and K. Taira. Effects of sidewalls and leading-edge blowing on flows over long rectangular cavities. *AIAA Journal*, 57(1):106–119, 2018. doi: 10.2514/1.J057413.

[42] B. George, L. Ukeiley, L. N. Cattafesta, and K. Taira. Control of three-dimensional cavity flow using leading-edge slot blowing. In *53rd AIAA Aerospace Sciences Meeting*, number 2015-1059, Kissimmee, FL, 5-9 January 2015. AIAA.

[43] F. R. Menter and Y. Egorov. The scale-adaptive simulation method for unsteady turbulent flow predictions. part 1: Theory and model description. *Flow, Turbulence and Combustion*, 85: 113–138, 2010. doi: 10.1007/s10494-010-9264-5.

[44] Y. Egorov, F. R. Menter, R. Lechner, and D. Cokljat. The scale-adaptive simulation method for unsteady turbulent flow predictions. part 2: Application to complex flows. *Flow, Turbulence and Combustion*, 85:139–165, 2010. doi: 10.1007/s10494-010-9265-4.

[45] F. R. Menter. *Best Practice: Scale-Resolving Simulations in ANSYS CFD*. ANSYS Inc., 2nd edition, November 2015.

[46] S.-H. Peng. M219 cavity flow. In W. Haase, M. Braza, and A. Revell, editors, *DESider – a European effort on hybrid RANS-LES modelling*, volume 103 of *Notes on numerical fluid mechanics and multidisciplinary design*, chapter 17, pages 270–285. Springer, 2009.

[47] T. Barth and D. Jespersen. The design and application of upwind schemes on unstructured meshes. In *27th Aerospace Sciences Meeting*, Reno, NV, 9-12 January 1989. doi: 10.2514/6.1989-366.

[48] B. P. Leonard. The ultimate conservative difference scheme applied to unsteady one-dimensional advection. *Computer Methods in Applied Mechanics and Engineering*, 88(1):17–74, 1991. doi: 10.1016/0045-7825(91)90232-U.

[49] R. A. Chaplin and T. J. Birch. The aero-acoustic environment within the weapons bay of a generic UCAV. In *30th AIAA Applied Aerodynamics Conference*, number AIAA-2012-3338, New Orleans, LA, 25-28 June 2012.

[50] S. J. Lawson and G. N. Barakos. Evaluation of DES for weapons bays in UCAVs. *Aerospace Science and Technology*, 14(6):397–414, September 2010. doi: 10.2514/6.2010-1425.

[51] P. D. Welch. The use of fast Fourier transform for the estimation of power spectra: A method based on time averaging over short, modified periodograms. *IEEE Transactions on Audio and Electroacoustics*, 15(2):70–73, June 1967. doi: 10.1109/TAU.1967.1161901.

[52] N. E. Huang, Z. Shen, S. R. Long, M. C. Wu, H. H. Shih, Q. Zheng, N.-C. Yen, C. C. Tung, and H. H. Liu. The empirical mode decomposition and the hilbert spectrum for nonlinear and non-stationary time series analysis. *Proceedings of the Royal Society A*, 454:903–995, 1998. doi: 10.1098/rspa.1998.0193.

[53] G. Wang, X.-Y. Chen, F.-L. Qiao, Z. Wu, and N. E. Huang. On intrinsic mode function. *Advances in Adaptive Data Analysis*, 2(3):277–293, 2010. doi: 10.1142/S1793536910000549.

[54] K. Dragomiretskiy and D. Zosso. Variational mode decomposition. *IEEE Transactions on Signal Processing*, 62(3):531–544, 2014. doi: 10.1109/TSP.2013.2288675.

[55] T. Liu, Z. Luo, J. Huang, and S. Yan. A comparative study of four kinds of adaptive decomposition algorithms and their applications. *Sensors*, 18(7):2120, 2018. doi: 10.3390/s18072120.

[56] Z. Wu and N. E. Huang. Ensemble empirical mode decomposition: A noise-assisted data analysis method. *Advances in Adaptive Data Analysis*, 1(1):1–41, 2009. doi: 10.1142/S1793536909000047.

[57] P. A. Davidson. *Turbulence: An Introduction for Scientists and Engineers*. Oxford University Press, 2nd edition, 2015. ISBN: 9780198722595.

[58] B. Khanal, K. Knowles, and A. J. Saddington. Computational investigation of cavity flow control using a passive device. *The Aeronautical Journal*, 116(1176):153–174, February 2012. doi: 10.1017/S0001924000006679.

[59] K. Luo, W. Zhe, Z. Xiao, and S. Fu. Improved delayed detached-eddy simulations of sawtooth spoiler control before supersonic cavity. *International Journal of Heat and Fluid Flow*, 63:172–189, 2017. doi: 10.1016/j.ijheatfluidflow.2017.01.012.

[60] N. Zhuang, F. S. Alvi, M. B. Alkislar, and C. Shih. Supersonic cavity flows and their control. *AIAA Journal*, 44(9):2118–2128, 2006. doi: 10.2514/1.14879.

[61] W. W. Bower, V. Kibens, A. W. Cary, F. S. Alvi, G. Raman, A. Annaswamy, and N. M. Malmuth. High-frequency excitation active flow control for high-speed weapon release (HIFEX). In *2nd AIAA Flow Control Conference*, number 2004-2513, Portland, OR, 28 June - 1 July 2004.

[62] C. Zhang, R. Li, Z. Xi, Z. Wan, and D. Sun. Effect of mach number on the mode transition for supersonic cavity flows. *Aerospace Science and Technology*, 106(106101):1–12, 2020. doi: 10.1016/j.ast.2020.106101.

[63] M. S. Mathias and M. A. F. Medeiros. The effect of incoming boundary layer thickness and mach number on linear and nonlinear rossiter modes in open cavity flows. *Theoretical and Computational Fluid Dynamics*, 35(4):495–513, May 2021. doi: 10.1007/s00162-021-00570-2.

Hilbert–Huang spectral analysis of cavity flows incorporating fluidic spoilers

Bacci, David

2022-10-07

Bacci D, Saddington AJ. (2023) Hilbert–Huang spectral analysis of cavity flows incorporating fluidic spoilers. AIAA Journal, Volume 61, Issue 1, January 2023, pp. 217-284
https://doi.org/10.2514/1.J061917